

MAROON: A Framework for the Joint Characterization of Near-Field High-Resolution Radar and Optical Depth Imaging Techniques

VANESSA WIRTH, Friedrich-Alexander-Universität Erlangen-Nürnberg, Germany

JOHANNA BRÄUNIG, Friedrich-Alexander-Universität Erlangen-Nürnberg, Germany

MARTIN VOSSIEK, Friedrich-Alexander-Universität Erlangen-Nürnberg, Germany

TIM WEYRICH*, Friedrich-Alexander-Universität Erlangen-Nürnberg, Germany and University College London, UK

MARC STAMMINGER*, Friedrich-Alexander-Universität Erlangen-Nürnberg, Germany

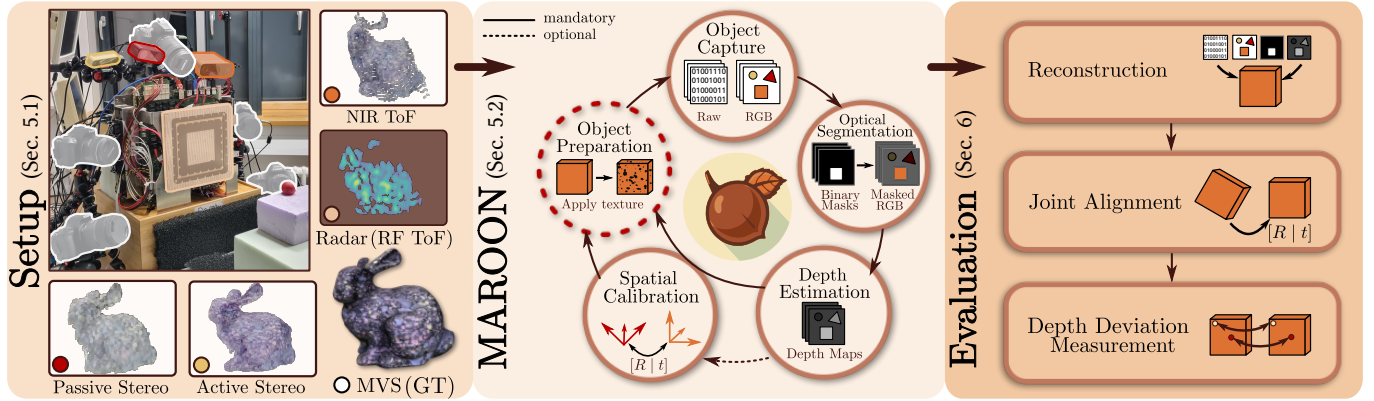


Fig. 1. Recent developments for near-field imaging radars enabled the acquisition of high-resolution depth images, and the sensors are now increasingly gaining attention as complementary modalities to optical depth sensing. Direct comparisons from our MAROON dataset, however, highlight significant differences between radar and optical reconstructions. This work employs the collected multimodal data of four depth imagers, depicted on the *left*, to systematically characterize these fundamental differences together with sensor-specific findings in a joint evaluation framework.

Utilizing the complementary strengths of wavelength-specific range or depth sensors is crucial for robust computer-assisted tasks such as autonomous driving. Despite this, there is still little research done at the intersection of optical depth sensors and radars operating close range, where the target is decimeters away from the sensors. Together with a growing interest in high-resolution imaging radars operating in the near field, the question arises how these sensors behave in comparison to their traditional optical counterparts. In this work, we take on the unique challenge of jointly characterizing depth imagers from both, the optical and radio-frequency domain using a multimodal spatial calibration. We collect data from four depth imagers, with three optical sensors of varying operation principle and an imaging radar. We provide a comprehensive evaluation of their depth measurements with respect to distinct object materials, geometries, and object-to-sensor distances. Specifically, we reveal scattering effects of partially transmissive materials and investigate the response of radio-frequency signals. All object measurements will be made public in form of a multimodal dataset, called MAROON.

Additional Key Words and Phrases: Time of Flight, Radar Imaging, Radio Frequency, mmWave Imaging, MIMO Radar, Depth Camera, Spatial Calibration, Multimodal Sensor Fusion, Dataset

1 Introduction

Real-world computer-assisted tasks, for instance in robotics and tracking applications, frequently require the immediate assessment of spatial information to accurately reason about the environment at a specific point in time, which has led to the development of several

single-view range and depth sensors. For autonomous driving, it has been shown that utilizing multimodal depth sensing techniques from both, the optical (lidar) and radio-frequency (radar) domain, can lead to superior performance and robustness in computer-assisted tasks [Velasco-Hernandez et al. 2020]. Due to its environment, the autonomous driving industry has traditionally concentrated on far-field range sensing, with an unambiguous range of several meters and beyond. As recent high-resolution radio-frequency technologies utilize the concept of *radar imaging* to produce 3D information in form of a depth map – similar to optical depth or RGB-D cameras – they also become more popular in close range, where the target of interest is up to a few decimeters away from the sensor; however, a comprehensive and detailed characterization of these radar imaging technologies, which frequently operate in the radar’s near field, has yet to be realized.

As part of this work, we devised a dataset **MAROON** (Multimodal Aligned Radio and Optical frequency Object Reconstructions in the Near Field) (cf. Section 5) that enables studying of different sensor modalities in direct comparison. As is immediately visible in Figure 1 (*left*), the reconstructions of near-field imaging radars appear fundamentally different in comparison to their well-researched counterparts in the optical domain.

A key advantage of radar is that it is insensitive to environmental light and can penetrate, for instance, fabric and dust. Following the success of Google’s project Soli [Lien et al. 2016] for gesture sensing, radars were utilized in close range for the detection of vital

*Both authors contributed equally to this research.

signs [Vilesov et al. 2022], activity recognition [Braeunig et al. 2023], people tracking [Zewge et al. 2019] and human body reconstruction [Chen et al. 2023, 2022]. With the growing trend towards larger antenna apertures to achieve high-resolution imaging [Chen et al. 2023; Schwarz et al. 2022], radars will more frequently operate in the near field, as determined by the Fraunhofer boundary condition [Selvan and Janaswamy 2017]. At the same time, characteristics of near-field radar are generally under-researched.

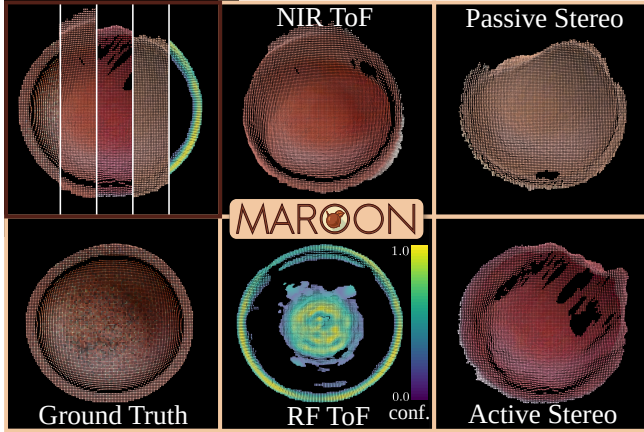


Fig. 2. Example data of the *Plunger* object from the MAROON dataset. In the *upper left*, all reconstructions are spatially aligned with respect to the RF ToF coordinate system. The RF ToF colorscale encodes the normalized reconstruction confidence (cf. Section 4.2.2).

Drawing on prior research about wavelength-specific strengths and weaknesses, this paper addresses the unique challenge of characterizing various optical depth-imaging techniques alongside a high-resolution multiple-input multiple-output (MIMO) imaging radar in the near field. The latter is interchangeably referred to as a radio-frequency (RF) Time-of-Flight (ToF) depth imager. To this end, we mutually calibrated sensors of four different depth sensing technologies, that is active and passive stereo, near-infrared (NIR) ToF, and RF ToF in the millimeter-wave range.

Using these sensors, we captured the comprehensive MAROON dataset of various household objects and construction materials, of which example data is shown in Figure 2. The dataset enables an exploration of sensor-specific characteristics with respect to various object materials, geometries and distances from the sensor. Furthermore, the spatial calibration enables a direct comparison of all sensor reconstructions in a common metrical space. We then compare these results to a reference ground truth reconstruction from a state-of-the-art multi-view stereo (MVS) system. To achieve this, we developed a joint sensor evaluation framework that measures reconstruction differences between sensors and ground truth using different metrics, and that provides supplementary visualizations tailored to identify sensor-specific trends across multiple objects. Our findings reveal fundamental differences between optical and RF sensors, as well as characteristics arising from specific depth measurement techniques within a single frequency domain. We

detail sensor-specific characteristics based on several key insights. First, by assessing deviation from the ground truth across different objects and object-to-sensor distances, we identify common sensor-specific trends. Given these, RF ToF reconstructions are found to be less complete compared to optical sensors. Lastly, we demonstrate that ToF sensors exhibit systematic depth errors resulting from interactions within partially transmissive media, such as subsurface scattering.

To summarize, our contributions are the following:

- A framework enabling the systematic comparative characterization of depth-sensing techniques in both, the optical and radio-frequency signal domain.
- A novel multimodal dataset, MAROON, comprising common objects in the near field, which were captured with the unique setup of four jointly calibrated depth sensors.
- We publicly release this dataset together with the raw radar measurements, thus enabling the community to explore different signal reconstruction and filtering techniques.¹
- A detailed analysis of trends and sensor-specific effects emerging from that dataset. This includes aspects of different object materials, geometries, and distances to the sensors, signal response and reconstruction quality of imaging radars, as well as ToF scattering effects of partially transmissive materials.

2 Related Work

While a considerable amount of literature exists on optical and RF depth sensors in isolation, no directly related work on the joint characterization of these two domains has been identified. Instead, the first two sections comprise an overview of existing research about sensor characteristics self-contained within a single frequency domain. We further address the sensor fusion of optical and RF sensors, since in that research direction the complementary strengths of the sensors are utilized as well.

2.1 Optical Depth Sensing

Depth cameras have been characterized with respect to a number of different aspects, and related work can be broadly classified into three categories: the sensor technologies, the capture environments, and the methods of comparison used to evaluate their performance.

Considering the sensor technologies, metrological research has been conducted in terms of optical ToF [Xiong et al. 2017; Zanuttigh et al. 2016] and active stereo [Giancola et al. 2018; Wang and Shih 2021]. Furthermore, working principles of passive stereo sensors have been widely addressed in computer vision algorithms [Szeliski 2022]. Similar to our work, Chiu et al. [2019] and Halmetschlager-Funek [2019] jointly characterize ToF and active stereo.

¹State-of-the-art methods for reconstruction and filtering will be publicly released together with the dataset viewer upon acceptance.

With respect to the capture environments, related work examined the effects of object material [Giancola et al. 2018; Halmetschlager-Funek et al. 2019; Hansard et al. 2012; Xiong et al. 2017], color [Giancola et al. 2018; Hansard et al. 2012; Xiong et al. 2017], texture [Hansard et al. 2012; Xiong et al. 2017] and distance to objects [Halmetschlager-Funek et al. 2019]. Furthermore, environmental lighting conditions [Halmetschlager-Funek et al. 2019] and multi-path effects [Giancola et al. 2018] were investigated. Specifically for ToF sensors, Wu et al. [2012] analyze multi-path effects originating from subsurface scattering and interreflections.

Moreover, we discuss related frameworks for jointly characterizing sensors. Halmetschlager-Funek et al. [2019] compare individually estimated depth values against manual measurements. Chiu et al. [2019] and Giancola et al. [2018] align the 3D data captured from sensors with real or synthetic ground truth data, respectively. Most similar to ours, Hansard et al. [2012] analyze ToF and structured light sensors using a spatial calibration and investigated object material, color, geometry, and texture using ground-truth data obtained from a structured light scanner.

2.2 Radio Wave Propagation and Range Sensing

So far, radio-frequency depth sensors (radar) were characterized in isolation. A more fundamental research direction examines the propagation of electromagnetic waves, which is the basis for RF ToF sensors. The general RF propagation behavior under different materials and geometries is measured by a parameter known as the radar cross section (RCS) [Knott et al. 2004]. The RCS approximates the returned ratio of a transmitted radio signal and was measured in relation to a variety of materials [Knott et al. 2004; Semkin et al. 2020], as well as in the context of humans [Deep et al. 2020; Marchetti et al. 2018]. Orthogonal research of Zhadobov et al. [2011] investigates the interaction of radio waves and human skin with respect to electromagnetic, thermal and biological aspects.

Moreover, studies of individual radar technologies have been conducted. Čopič Pucihar et al. [2022] evaluate the recognition of hand gestures using millimeter-wave radars in the presence of various materials. Wei et al. [2021] characterize imaging radars with respect to the geometry of metal objects in the context of security scanning. Furthermore, Bhutani et al. [2022] examine millimeter-wave radars at different frequencies, whereas Jha et al. [2018] analyze differences in their radiation between the near field and the far field. Sun et al. [2020] provide an overview of MIMO radars for autonomous driving, together with the characterization of their wave forms. Lastly, Ahmed [2021] presents millimeter-wave MIMO radar imaging systems in the context of security screening. To the best of our knowledge, no comprehensive characterization in conjunction with optical technologies has been done so far. Additionally, the existing efforts have been limited in scope with regard to RF depth sensing in the near field.

2.3 Fusion of RF and Optical Sensors in Close Range

Knowledge about complementary strengths is important for both, sensor characterization and sensor fusion. Research on multimodal sensor fusion in close range is very limited and mostly focused on capturing humans.

Zewge et al. [2019] perform people tracking with a 4×3 MIMO radar and an active stereo camera. Similarly, Lee et al. [2023] propose a method for human pose estimation, which utilizes the data acquired from two 4×3 MIMO radars synchronized with a monocular RGB camera. Both works do not utilize radar imaging methods due to the limited resolution. More similar to ours, Chen et al. [2023] use a high resolution 48×48 MIMO radar and an RGB camera for human body reconstruction.

Furthermore, we address related datasets. Lim et al. [2021] introduce RaDiCaL, an indoor and outdoor dataset of multiple people and objects, captured with a 4×3 MIMO imaging radar and an active stereo camera. In the context of human body reconstruction, Chen et al. [2022] propose the mmBody benchmark that was captured with a 48×48 MIMO radar and an RGB camera.

3 Preliminaries

As different research communities partially differ in their terminology, this paper pursues a unified terminology, summarized in the table below and used in the remainder of this paper.

Depth Imager. A sensor that, directly or indirectly, captures a depth image D of resolution $W \times H$, where each pixel (u, v) contains a depth value d measured along the axis perpendicular to the image plane. The depth may be indirectly measured from range and pixel position. We show the difference between range and depth in Figure 3.

Transmitter and Receiver. Optical receivers are small cells of image sensors, with a direct mapping to pixels. Transmitters are commonly LEDs or projectors. RF sensors have transmitting (TX) and receiving (RX) antennas.

Sensor. Describes all physical parts required for depth sensing and their spatial arrangement. Optical sensors typically consist of one or two cameras. Active sensors contain an additional illumination unit. RF sensors usually have one or more antenna arrays in different arrangements.

Depth Image Resolution $W \times H$. The number of depth samples computed from the incoming signal. In cameras, the depth samples are directly computed for each pixel, i.e., each receiver. MIMO imaging radars apply signal post-processing to compute depth from the signal diversity at different receiver positions. Hence, the image resolution is not directly affected by the number of receivers but by the signal processing parameters such as the voxel density (cf. Section 4.2.2). While, in theory, the depth image resolution can be indefinitely high, in practice it is limited by the spatial resolution.

Spatial Resolution δ . The term resolution has several definitions. Here, we explicitly refer to spatial resolution as the minimum distance between two points in space that can be resolved from the received signal. Lower spatial resolution means higher minimum resolvable distance, so more incorrect measurements are made when points become inseparable, as seen in Figure 3. Spatial resolution is a theoretical measure, and external factors such as the sensor design can affect its *effective* resolution. Literature about traditional multi-static RF ToF sensors divides spatial resolution

into range resolution (δ_r), and cross-range resolution along the horizontal (δ_h) and vertical (δ_v) axes, respectively. While δ_h and δ_v are measured at a specific range, a more general formulation is the angular resolution, often referred to as azimuth (ω_h) and elevation (ω_v) resolution [Willis and Griffiths 2007]. Literature from the optical domain shares a similar definition, however, with a different terminology and refers to depth resolution [Zanuttigh et al. 2016] (δ_z) and pixel resolution (δ_h, δ_v) instead. Similar to traditional RF ToF sensors, optical sensors assume that the target is situated in the far field, where depth is approximately the same as range and, hence, $\delta_z \approx \delta_r$. We note that this assumption does not generally hold in the near field. Due to the concept of an expanded antenna aperture with multiple transmitters and receivers, the resolution of near-field MIMO imaging radars is defined with respect to the three orthogonal axes x, y, z . In these, z refers to the depth axis and x, y are parallel to the antenna aperture. Contrary to their difference in definition, they share the same terminology as far-field RF ToF sensors such that δ_z is referred to as range resolution and $\delta_{x,y}$ is the cross-range [Ahmed 2014] or lateral [Ahmed 2021] resolution, respectively. We illustrate the respective definitions that are used for optical ($\delta_h, \delta_v, \delta_r$) and RF sensors ($\delta_x, \delta_y, \delta_z$) in Figure 3. For simplicity, we define spatial resolution only for the sensor center, where depth and range are approximately the same, such that $\delta_z \approx \delta_r$ and $\delta_{x,y} \approx \delta_{h,v}$.

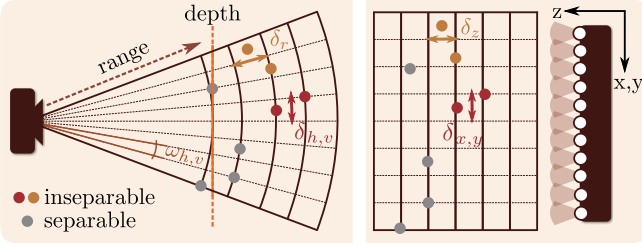


Fig. 3. Visualization of the effects caused by limited spatial resolution for multiple point targets. Optical sensors (left) have similar definitions as far-field RF ToF sensors and divide spatial resolution into depth $\delta_r \approx \delta_z$ and pixel resolution, $\delta_{h,v}$. Contrary to that, near-field imaging radars (right) refer to range δ_z and cross-range $\delta_{x,y}$ resolution. We define $\delta_z \approx \delta_r$ and $\delta_{x,y} \approx \delta_{h,v}$ for the sensor center, yet emphasize the conceptual difference between range and depth.

4 Working Principles of Depth Imagers

In order to gain insight into the fundamental differences between optical and RF sensors, the first section characterizes wavelength-specific signal propagation. This is followed by an outline of the hardware design choices that are made for optical and RF depth imagers. After this, the working principles of the sensor technologies that are used in our experiments are discussed.

4.1 Characterization of Wavelength

Depth imagers are susceptible to the received, and optionally transmitted, signal wavelength. The wavelength affects both, the interaction of the signal with matter and the design of the sensor hardware and depth sensing algorithms. In this section we elaborate on both

aspects, with a particular focus on the near-infrared light spectrum and the millimeter-wave (mmWave) radio-frequency spectrum.

NIR signals have a wavelength in the nanometer range. Given their high energy and strong interaction with matter, signal reflection or absorption is common, with scattering and non-diffractive phenomena dominating across most materials. Indirect effects on interactions with matter, therefore, often play a subordinate role, such that short propagation paths can be expected. Moreover, NIR light is pervasive in the environment, rendering optical technologies susceptible to external interference.

As suggested by their name, the wavelength of mmWave signals is longer by comparison. The low energy and reduced interaction with matter result in lower absorption and reflection, while there is a higher chance of a signal being transmitted through material. Specifically, the penetration depth of millimeter waves through matter is dependent on material parameters, such as, the resistivity and permittivity. For instance, the signals of security scanners can penetrate fabric but are primarily reflected on contact with metal objects [Ahmed 2021]. Furthermore, diffraction is more common with millimeter waves. This allows waves to bend around objects. Due to the aforementioned phenomena, the propagation paths of signals from active RF sensors are typically longer than of signals from optical sensors. Lastly, mmWave depth imagers operate with reduced external interference, as there are few natural microwave sources in the environment.

Due to the wavelength, the sensor design of RF sensors is inherently different from that of optical sensors. As stated by the general formulation of the Rayleigh criterion, the focus capacity and, hence, angular resolution ω of a sensor is limited by the signal wavelength λ and the size of the sensor's aperture L [Hasch et al. 2012]:

$$\omega_{x,y} = 1.22 \frac{\lambda}{L_{x,y}}. \quad (1)$$

Optical sensors utilize camera lenses to refract the received signal, which enable a precise focus onto nanometer-sized pixels and, at the same time, exhibit a high angular resolution. In the context of the mmWave domain, a camera analogue can be conceptualized as a single-input multiple-output (SIMO) radar, which is to say, a sensor comprising a single transmitter and multiple receivers. As indicated by Equation 1, mmWave sensors have a significantly lower angular resolution than optical sensors. Thus, high-resolution SIMO radars require comparably large antenna arrays with large lenses, which has proven to be impractical. Instead, high-resolution RF imaging sensors often are synthetic aperture radars (SAR), which use digital beamforming to focus. They utilize the angle diversity from distinct transmitter and receiver positions, which form a virtual aperture of size L , to increase the angular resolution [Bliss and Forsythe 2003] and require fewer antennas compared to SIMO systems. The majority of near-field SAR radars is implemented with MIMO arrays, that is, with multiple transmitters and receivers.

4.2 Depth Sensing Methods

In this section, we address the working principle of both optical and RF-based depth sensing methods used in our experiments. The content is organized in two categories: spatially resolved and time-resolved depth sensing, which are both depicted in Figure 4.

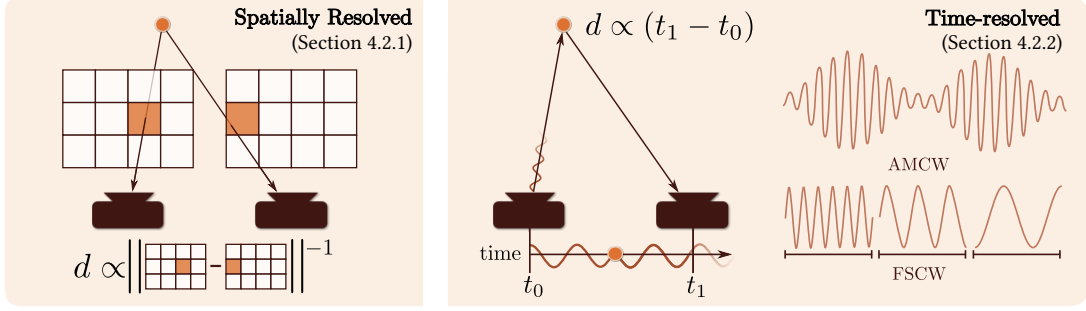


Fig. 4. Overview of the two depth sensing categories considered in this work. Spatially resolved methods compute the depth from disparity in the pixel positions. Time-resolved methods measure the depth through the round-trip propagation time of the received continuous wave (CW) signal. The types of wave forms utilized in our experiments are amplitude-modulated continuous wave (AMCW) and frequency-stepped continuous wave (FSCW).

4.2.1 Spatially Resolved Depth Sensing. Spatially resolved depth imagers compute the point-wise depth from the respective pixel position in the image. In the following, we particularly address passive or active stereo(scopy) sensors.

Passive stereo sensors commonly utilize two cameras with a known relative spatial position to identify surface points in their respective images, a process known as *correspondence* or *stereo matching* [Szeliski 2022]. Given a correspondence pair of two pixels, the respective depth of this surface point is computed from their disparity. The quality of the correspondence matches affects the depth and accuracy of the results. Ambiguities in correspondence can arise due to textureless regions, poor lighting, motion or lens blur. Similarly, stereo matching can fail in terms of view-dependent effects or partial surface occlusions from one of the two receivers.

Active stereo sensors assist correspondence finding with an illumination unit that projects a pattern onto the target, usually in the NIR range, captured by the two cameras. The signal-multiplexed [Zanuttigh et al. 2016] pattern assists epipolar correspondence matching in addition to shading and texture cues, improving depth quality in textureless regions and low light. However, challenges include pattern distortions and signal oversaturation at the NIR receiver in bright conditions. Further details on spatially resolved depth sensors are provided in the supplementary material.

4.2.2 Time-Resolved Sensors (Time of Flight). Time of Flight is an active depth sensing method, in which depth is derived from the round-trip propagation time that it takes for a signal to be transmitted and received. The majority of ToF sensors utilized in the near field employ continuous wave (CW) signal modulations, which measure time based on the relative phase shift $\Delta\phi$ between the transmitted and received signal. The depth is derived from the range r , which is measured by [Zanuttigh et al. 2016]:

$$r = c \frac{\Delta\phi}{2\pi f} . \quad (2)$$

The signal frequency is denoted as f , and c is the speed of light in vacuum, which closely matches that of light in air. For further details about the operating principle, we refer to the supplementary material. ToF technologies employ a simplified model for range sensing, which assumes that targets are diffuse scatterers, with each signal reflecting directly from the first target. As a result, these technologies

are sensitive to multi-path interference, where signals propagate indirectly in multiple directions before reaching the receiver. In Section 8, we identify partially transmissive materials as a major cause of such interference. Furthermore, the unambiguous range of resolving $\Delta\phi$ is limited to the periodicity of the sinusoidal CW signal. To extend this range, the carrier signal can be modulated over time. In our experiments, we use ToF sensors with amplitude-modulated continuous wave (AMCW) and frequency-stepped continuous wave (FSCW) signal modulations, which are illustrated in Figure 4. Up next, we will discuss the operating principles of these depth sensing methods.

NIR AMCW Time of Flight. AMCW ToF algorithms usually operate on the SIMO principle, as they do not require as expensive sensor apertures as imaging radars, and often have more receivers and transmitters than can be effectively managed computationally in MIMO depth estimation algorithms [Zanuttigh et al. 2016]. They modulate the amplitude A of a carrier signal over time t using a repetitive modulation signal s_m such that the transmitted signal s_t can be described as:

$$s_t(t) = \underbrace{s_m(t)}_A \cdot \cos(2\pi f t + \phi_c) . \quad (3)$$

A constant phase offset is described by ϕ_c . To extract the phase shift from the received signal s_r , it is cross-correlated with a so-called signal hypothesis s_h [Zanuttigh et al. 2016]:

$$c_r(t) = \int_0^{T_m} s_r(t) s_h(t + t') dt' . \quad (4)$$

T_m is the period of the modulation signal s_m . Commonly, s_h is chosen as the currently transmitted signal s_t such that c_r describes the signal similarity from which the relative phase shift to s_r is inferred. Extracting this shift requires solving a multivariable equation system with parameters such as the received amplitude and external illumination. To achieve this, c_r and, consequently, s_r are commonly sampled at four points within T_m (four-bucket-method) [Giancola et al. 2018]. During the acquisition of those samples, AMCW ToF is affected by environmental changes, such as varying external NIR illumination and motion. Similar to active stereo, oversaturation of the NIR receiver may cause invalid signal responses.

MIMO FSCW Time of Flight. Given the frequency band $b = f_{\max} - f_{\min}$, FSCW ToF sensors iteratively send N_f signals of one frequency in steps of $\Delta f = b/N_f$ [Bräunig et al. 2023b]. More specifically, the transmitted signal s_t of one capture can be described as:

$$s_t(t) = A \cdot \cos(2\pi t f_m(n) + \phi_c) \text{ with } n = \lfloor t/\Delta t \rfloor \quad (5)$$

$$f_m(n) = f_{\min} + \left(n \bmod N_f \right) \Delta f. \quad (6)$$

We denote the time window of one frequency step as Δt . Time-division multiplexing (TDM) avoids signal interference and facilitates the separation of the received signal into its originating transmitter and frequency components. SAR signal processing computes the depth d and the pixel position (u, v) from the phase shift and the angular diversity originating from multiple transmitting and receiving positions. For MIMO imaging radars, the state-of-the-art algorithm of *backprojection* (BP) [Ahmed 2021] computes confidence values about a target's presence in 3D space. This is achieved on the basis of local feature distributions within a volume based on the integrated signal of each RX-TX antenna pair. Similar to the previous section, the BP algorithm computes a correlation between the received signal s_r and a signal hypothesis s_h :

$$c_{BP}(x, y, z) = \sum_{n=1}^{N_f} \sum_{i=1}^{N_{RX}} \sum_{j=1}^{N_{TX}} s_r(f_n, r_i, t_j) s_h(f_n, r_i, t_j, \mathbf{p}). \quad (7)$$

A hypothesis is made on the basis of the transmitted signal, which is assumed to reflect at a point $\mathbf{p} \in \mathbb{R}^3$ in the sensor coordinate system, commonly sampled from a voxel grid of size $N_v = N_x \times N_y \times N_z$. The demodulated received signal, s_r , varies in transmit frequency $f_n = f_m(n)$, transmitter position $t_j \in \mathbb{R}^3$, and receiver position $r_i \in \mathbb{R}^3$. We further denote the numbers of transmitters and receivers as N_{TX} , and N_{RX} , respectively. Generally, hypotheses are made by assuming the signal propagation is following the so-called Born approximation [Ahmed 2014]. The result of the above equation is a complex phasor, c_{BP} , with its absolute value representing the confidence of a target's presence, which is visualized in Figure 2. It is calculated from s_r and s_h , which are analytic signals in complex notation. More details are given by Ahmed [2021]. To compute a 2D depth map from the 3D voxel grid, an orthogonal *maximum (intensity) projection* [Bräunig et al. 2023b] is performed for each pixel $(u, v) = (x, y)$ along the cross-depth axes of the voxel grid:

$$d(u, v) = \underset{z}{\operatorname{argmax}} \|c_{BP}(x, y, z)\|_2. \quad (8)$$

Besides projection, the confidence values are used as thresholds for depth filtering, that is, to distinguish target depth from sidelobes and background noise. The absolute value of the confidence c_{BP} depends on both, the received phase and amplitude. Besides the depth, reasons for varying amplitude and phase over different object materials and geometries are manifold, and further insights will be given in Section 9. As a result, it is challenging to generalize the depth filtering process for unknown objects. Similar to NIR AMCW ToF, a MIMO FSCW ToF sensor requires multiple signal samples to compute depth and, thus, is sensitive to environmental changes during capture.

5 The MAROON Dataset

The capture of the MAROON dataset allows for a comprehensive analysis with respect to the characteristics of the four previously described depth sensing techniques. This section outlines the capture setup and data acquisition pipeline, depicted in Figure 1, to aid future research on the publicly accessible data. Four single-view depth sensors are used in our experiments: Stereolabs ZED X [Stereolabs 2023] (Passive Stereo), Intel Realsense D435i [Intel 2023] (Active Stereo), Microsoft Azure Kinect [Microsoft 2022] (NIR ToF), and a submodule of Rohde & Schwarz's QAR50 [Rohde & Schwarz 2023] (RF ToF). Example data captured from these sensors is visualized in Figure 2.

5.1 Sensor Setup

Our sensor setup consists of four mounted single-view depth sensors and a ground truth (GT) optical multi-view stereo (MVS) system comprising five calibrated DSLR cameras, which are depicted on the *left* in Figure 1. While all single-view sensors are designed to achieve an optimal balance between depth quality and acquisition time, the MVS system employs an offline reconstruction process that is specifically optimized for depth quality. In summary, eight cameras are mounted on tripods and arranged around the MIMO imaging radar on a desk, thereby maximizing the area of intersection of each sensor's field of view, to ensure similar object visibility. All sensors and the GT system are time-synchronized, either through hardware or software, to capture the object at the same moment.

Prior to capture, the object is positioned in the center of the squared radar aperture, and approximately at the center of the joint field-of-view intersection, propped up with boards crafted from styrofoam — a material that is considered to be nearly fully penetrated by the RF signal — to prevent external interference of radio waves from other sources in the vicinity, apart from the object of interest. For similar reasons, absorbers are placed behind the object of interest. Similarly, for optical sensors a loose black cloth, which is penetrated by RF signals, is suspended in front of the absorbers to visually occlude the room's background. The sensor settings are chosen with respect to a trade-off between fair sensor comparability and practical applicability. More details can be found in the supplementary material. An overview of the chosen settings, together with relevant sensor parameters, is given in Table 1.

5.2 Data Acquisition Pipeline

To examine the characteristics of various objects in relation to different materials, geometries, and distances from the sensor, we recorded the MAROON dataset, which comprises static and quasi-static targets captured from all sensors simultaneously. With respect to the order of steps described in Figure 1 (*middle*), we will now continue to elaborate on the details of the acquisition pipeline.

Spatial Calibration. We spatially aligned the coordinate systems of each depth imager using the calibration method by Wirth et al. [2024]. In this method, four respective spherical objects of styrofoam and metal, tailored to the visibility of optical and RF sensors, are captured. In the sensor-specific reconstructions, these spheres are automatically located and jointly aligned using spatial registration. This approach enables a direct comparison of the object

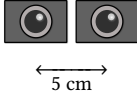
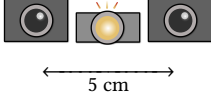
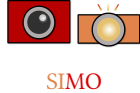
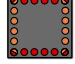
		ZED X Mini (2.2 mm) [Stereolabs 2023]	Realsense D435i [Intel 2023]	Azure Kinect [Microsoft 2022]	QAR5 (Submodule) [Rohde & Schwarz 2023]
Manufacturer		Stereolabs	Intel	Microsoft	Rohde & Schwarz
Depth Sensing Technology		Passive Stereoscopy	Active Stereoscopy	Time of Flight (NIR)	Time of Flight (RF)
Arrangement				 SIMO	 MIMO (square)
Capture Frame Rate		30 fps	30 fps	30 fps	≈ 70 fps*
Transmitters	Type	—	Laser Projector	LED Array	TDM Antenna Array
	Array Size	—	—	—	2×47 TX ↓
	Wavelength	—	840–860 nm	860 nm	3.6–4.2 mm
	Frequency	—	≈ 353 THz	≈ 353 THz	72–82 GHz
	Signal Modulation	—	Spatial Multiplexing	AMCW	FSCW ($N_f = 128$)
Receivers	Type	Image sensor	Image sensor	Image Sensor	Antenna Array
	Array Size	2×1928×1208 px	2×1280×800 px	1024×1024 px	2×47 RX ↔
	Spatial Size*	2×5.8×3.6 mm	2×3.8×2.4 mm	3.6×3.6 mm	2×13.8 cm
Depth Image Resolution		1920×1080 px	1280×720 px	640×576 px	301×301 px
Spatial Resolution*	30 cm	0.30×0.39×1.34 mm	0.36×0.42×0.21 mm	0.61×0.59× ≤ 2.0 mm	4.08×4.08×11.08 mm
	40 cm	0.40×0.52×2.38 mm	0.47×0.56×0.38 mm	0.82×0.79× ≤ 2.0 mm	5.38×5.38×12.44 mm
	50 cm	0.50×0.65×3.72 mm	0.59×0.70×0.59 mm	1.02×0.98× ≤ 2.0 mm	6.69×6.69×13.23 mm

Table 1. Overview of the sensors and their parameters used in our experiments. Rows with * indicate information not directly given by the manufacturer. δ_x and δ_y of camera-based systems is approximately determined from the per-pixel field of view. Spatial resolution formulae are provided in the supplementary material. Due to missing data for the Azure Kinect, δ_z is assumed to be theoretically higher than the depth accuracy given in [Bamji et al. 2018].

reconstructions in a metrical space. Calibration errors are expected to be in 1–2 mm range with respect to the Chamfer distance, in analogy with Wirth et al. [2024].

The five DSLR cameras of the MVS system are treated as a unified sensor with a common coordinate system, which is spatially calibrated with that of the depth imagers. The camera extrinsic and intrinsic parameters of the MVS system are determined from images capturing a conventional optical calibration target with a checkerboard pattern. For this, we use the software provided by Agisoft Metashape. Remaining calibration errors exhibit a root mean square reprojection error of 0.38 px, averaged over all camera calibrations performed during the dataset capture.

Object Preparation and Capture. The reconstruction method of MVS is similar to passive stereo imagers. Hence, inaccurate reconstructions can be the result when dealing with textureless and view-dependent object materials. To circumvent this limitation, we implement a distinct capture process for particularly challenging objects to generate more reliable GT reconstructions. Once the object has been captured by all depth imagers, a thin multicolored speckle pattern is applied using water colors that assists the correspondence finding by a subsequent MVS-only capture. In order to ensure exact alignment between that GT reconstruction and other imaging modalities, the speckle is applied in situ without moving the object.

In total, each object is recorded at three different distances to the MIMO imaging radar of 30 cm, 40 cm, and 50 cm, respectively. The remaining depth imagers are situated behind the radar. Their corresponding object-to-sensor distance is determined from the distance to the radar and from the relative position between each optical sensor and the imaging radar, which is given by the calibration parameters. Based on the Euclidean norm of the mean translation across all calibrations conducted, we report an additional object-to-sensor distance of +8 cm (Azure Kinect), +6 cm (Realsense D435i), and +5 cm (ZED X Mini), respectively. We record 20 frames for each optical sensor and 10 radar frames. In total, we capture 45 objects and list further statistics about the dataset in Table 2.

Optical Segmentation. To perform an accurate and precise object-centric sensor evaluation, it is essential to isolate the estimated object depth from the background. For optical systems, we acquire segmentation masks by performing a semi-automatic foreground-background segmentation. Given that all depth imagers capture RGB images — either for depth estimation or via a separate calibrated camera — we first segment the RGB images using manually defined object labels in conjunction with Grounded-SAM [Ren et al. 2024]. This generates a binary segmentation mask of the object, \mathbf{M} , where all valid pixels (u, v) are included in $\mathbf{M}^+(u, v) = \{\mathbf{M}(u, v) > 0\}$. We then manually correct failure cases in the resulting segmentation masks. The same procedure is employed to MVS images to produce masked GT reconstructions. For the imaging radar, the voxel volume

of the BP algorithm (Equation 7) is constrained to enclose only the object of interest. In this way, segmentation masks are automatically determined from the valid pixels remaining after depth estimation.

Depth Estimation. We perform the BP algorithm for the imaging radar on a $301 \times 301 \times 201$ voxel grid with centers sampled in 1 mm steps within a $15 \times 15 \times 40 \text{ cm}^3$ volume around the object center. Subsequently, we apply maximum projection (Equation 8) to acquire a 2D projection of the depth as well as a 2D confidence map. Using the latter, we filter out depth values according to a threshold of -14 dB relative to the maximum value. As mentioned in Section 4.2.2, such thresholding is challenging for unknown objects (see supplementary). We chose this threshold empirically over all objects in the dataset, aiming at a good balance between pruning of noise and retention of object details. We encourage interested readers to experiment with different thresholds, using the raw radar data available in our dataset. The filtered result is stored as an orthographic depth map. Lastly, the GT surface of the object is collected in a mesh representation after performing MVS reconstruction (using Agisoft Metashape) and Laplacian smoothing. For optical sensors, we directly use the signal processing algorithms provided by the manufacturer.

Statistics	MAROON
# objects	45
# static objects	41
# quasi-static objects	4
# prepared speckled objects	14
# captures (# objects \times 3 distances)	135
# total / unique optical depth frames	8100 / 405
# total / unique RF depth frames	1350 / 135

Table 2. Statistics of the MAROON dataset. Assuming that all captured objects are static, the number of total frames include duplicate captures, possibly varying in random depth noise, while the unique frames only contain one capture per object of each sensor.

6 Evaluation

In this section, we compare the reconstructions produced by the four presented depth imagers with a ground-truth reconstruction in a common metric space and describe the methods used in this process. Subsequently, the results of these methods are presented.

6.1 Methods

In accordance with the order in Figure 1 (right), the necessary steps for evaluation are explained.

Reconstruction. We acquire a point cloud of the object’s surface utilizing the 2D depth and auxiliary data provided by MAROON. For a given pixel position (u, v) and its corresponding depth d from an optical depth sensor, we first verify its validity using the segmentation map of the same resolution — a step that has already been performed for radar during depth filtering. Subsequently we project each valid triple (u, v, d) back into 3D space using the given

transformation matrix $T \in \mathbb{R}^{4 \times 4}$:

$$\begin{pmatrix} x \\ y \\ d \\ 1 \end{pmatrix} = \underbrace{\begin{pmatrix} I & t \\ 0 & 0 & 0 & 1 \end{pmatrix}}_{T^{-1}}^{-1} \begin{pmatrix} u \cdot a \\ v \cdot a \\ d \\ 1 \end{pmatrix}. \quad (9)$$

For all optical depth imagers, this equation is the inverse of a perspective transformation with intrinsic camera matrix $I \in \mathbb{R}^{3 \times 3}$, pixel offset vector $t \in \mathbb{R}^3 = \mathbf{0}$ and $a = d$. Analogously for radar data, the equation is the inverse of an orthographic transformation with a scale matrix I , pixel offset t , and $a = 1$.

During evaluation, we average valid depth values across 10 frames for static objects to incorporate temporal characteristics and reduce random noise. We do not average quasi-static objects (e.g., human hands) and instead take the first frame, as it is closest to the point in time where the GT captures have been taken.

Joint Alignment. To estimate the deviation of a sensor reconstruction $R_s \in \mathbb{R}^{M \times 3}$ from the GT, $R_g \in \mathbb{R}^{N \times 3}$, we use the previously determined spatial calibration parameters $K_{g \rightarrow s} \in \mathbb{R}^{4 \times 4}$ to transform R_g from the GT space g into the sensor space s :

$$\tilde{R}_g^s = \tilde{R}_g K_{g \rightarrow s}^T. \quad (10)$$

\tilde{R} denotes the homogeneous version of R . We use the notation R^* to indicate a reconstruction that has been transformed to sensor space $*$.

Depth Deviation Measurement. For each object, we compute the point-wise deviation between a sensor and the GT reconstruction with respect to two metrics: one-sided Chamfer distance and one-sided projective error. The one-sided Chamfer distance, C , is computed per point $p \in \mathbb{R}^3$ in the source point cloud $P \in \mathbb{R}^{N \times 3}$ with respect to the distance to the nearest point $q \in \mathbb{R}^3$ in the destination point cloud $Q \in \mathbb{R}^{M \times 3}$:

$$C_p(Q) = \min_{q \in Q} \|p - q\|_2. \quad (11)$$

The one-sided projective depth error P is computed per pixel (u, v) of two depth maps $D \in \mathbb{R}^{W \times H}$ and $F \in \mathbb{R}^{W \times H}$ of a common image plane:

$$P_{u,v}(D, F) = |D(u, v) - F(u, v)|. \quad (12)$$

For both, C and P , the respective subscripts p and u, v are used as placeholders to denote the points and pixels used in the metric computation. We compute both metric types for each reconstruction pair of a sensor, R_s , and the GT, R_g . Since the one-sided Chamfer distances are sensitive to the point cloud density, we uniformly sample the points from the sensor and the GT with respect to a common image pixel grid. We achieve this by, first, computing a simulated depth map \tilde{D}_g^s in the image space of the sensor s and, second, reconstructing \tilde{R}_g^s from this depth map, using Equation 9 with the sensor-specific transformation T_s . The simulated depth map is computed by rasterizing a triangulated representation of R_g^s with respect to T_s . In

this way, we also discard points in optical sensors R_g^s that are not visible in the view of camera s . The resulting depth map \widehat{D}_g^s is additionally used to measure the projective error. To summarize, we compute:

C_g	Chamfer distance ground truth. $\forall g \in \widehat{R}_g^s : C_g(R_s)$
C_s	Chamfer distance sensor. $\forall s \in R_s : C_s(\widehat{R}_g^s)$
P	Projective error. $\forall (u, v) \in M^+(u, v) : P_{u,v}(D_s, \widehat{D}_g^s)$ for $M = M_s \cap \widehat{M}_g^s$, where $M_s = \{D_s > 0\}$ and $\widehat{M}_g^s = \{\widehat{D}_g^s > 0\}$ describe the intersection masks of valid pixels from the sensor and the projected GT, respectively.
P_e	Projective error with erosion. $\forall (u, v) \in M_e^+(u, v) : P_{u,v}(D_s, \widehat{D}_g^s)$ for $M_e = M_s \cap f(\widehat{M}_g^s)$, where $f(\widehat{M}_g^s)$ is a function performing mask erosion using a kernel size of $K \times K$ pixels. The size $K \in [0, 20]$ is semi-manually selected for each object and sensor, and included together with other evaluation metadata in the release of our dataset.

Metric Type	Silhouette Noise	Missing Surfaces	3D Error	Depth Error
C _g	—	✓	✓	—
C _s	✓	—	✓	—
P	✓	—	—	✓
P _e	—	—	—	✓

Table 3. Categorization of the presented metrics with respect to their sensitivities. In addition to depth, a 3D error evaluates errors along the cross-depth axes.

6.2 Results

In this section, we first present the evaluation results, quantified using four complementary metrics: C_g, C_s, P, and P_e. Each metric is sensitive to different aspects, as detailed in Table 3. Important to note is that the computed quantities do not perfectly reflect the absolute depth error in the real world, due to the limitations of our experimental setup, which is constrained by the accuracy of the GT system and the spatial calibration. Instead, the results should be interpreted as depth deviation from the ground truth, referred to as sensor-GT deviation. We begin by presenting the sensor-GT deviation results in relation to various objects and different object-to-sensor distances. Given that near-field imaging radars are less explored compared to optical depth sensors, we dedicate the latter part of this section to the radio-frequency signal response. Finally, we note that in this section the results are objectively presented, reserving further interpretations for subsequent sections, where they will be discussed from a general perspective (Section 7), with specific attention to partially transmissive media (Section 8), and focusing on the RF signal response (Section 9).

6.2.1 Depth Deviation at Single and Multiple Object Distances. In Table 4, we list the mean μ and standard deviation σ of each metric type with respect to 12 selected objects from the MAROON dataset. These objects were positioned at an object-to-sensor distance of

30 cm. We provide object images and a comprehensive evaluation of all 45 objects in the supplementary material. For completeness, we give a brief overview of the overall statistics by investigating the number of best and worst results across all objects for μ , respectively:

- RF ToF: performs worst in C_g
- NIR ToF: performs worst in C_s, P, P_e
- Active Stereo: performs best in C_g, C_s, P, P_e
- Passive Stereo: performs neither best or worst

To give an intuition on relative depth deviations between sensors, we present the median, mean, and standard deviation, denoted as $\widetilde{\mu}/\mu (\pm\sigma)$, calculated across the differences in metric values for all pairwise sensor combinations. The results for each metric type are:

- C_g: 0.23 cm/0.48 cm (± 0.61 cm)
- C_s: 0.19 cm/1.06 cm (± 3.53 cm)
- P: 0.34 cm/1.58 cm (± 4.36 cm)
- P_e: 0.31 cm/1.78 cm (± 5.14 cm)

Additionally, we illustrate the distribution of the depth deviation across all objects for varying placement distances of 30 cm, 40 cm, and 50 cm. The results are displayed as boxplots in Figure 5.

6.2.2 RF Signal Response at Single Object Distance. In addition to the phase shift, the point-wise confidence of the backprojection algorithm for RF ToF is significantly affected by the signal amplitude; however, disentangling amplitude and phase in the presence of signal interference imposes the same challenges that arise from recovering the phase shift itself. To avoid inducing additional bias through the assumptions made in signal processing, we investigate the unprocessed signal response in the MIMO imaging radar across multiple objects. For each object at 30 cm object-to-sensor distance, we compute the mean absolute value out of all complex phasors received from the raw signal of size $N_{RX} \times N_{TX} \times N_f$, averaged over 10 frames. We refer to this quantity as signal *magnitude*, emphasizing the difference from signal amplitude.

To investigate correlations between signal response and reconstruction quality, we analyzed the signal magnitude relative to the depth deviation from ground truth, expressed as the mean of C_g. These findings are shown on the *left* in Figure 6. We further differentiate between *signal magnitude* (upper row) and *depth deviation* (bottom row), examining their relationships with respect to object material, geometry, and size from left to right. *Object materials* are categorized into six classes, with detailed information available in the supplementary material. The goal of this classification is to highlight material differences on a coarse level, noting the large object variety that still persists within one material class. The *object geometry* is quantified by the median angle in degrees between the point-wise surface normals of the GT reconstruction and the depth direction (along the z -axis) of the imaging radar. As we positioned the objects to align their primary orientation with the viewing direction of the planar square-shaped antenna aperture — which particularly becomes important for flat objects — the median angle mainly reflects geometric complexity, with objects having a higher surface incidence angle showing larger portions oriented away. *Object size* is determined by the relative surface area compared to the radar antenna aperture. It is computed from the fraction of the object’s 2D axis-aligned bounding box A (in the x - and y -axis) inside

	Metric Type	Cardboard	Sponge	Scrubber	Plushie	Tape Dispenser	Statue
RF ToF	C_g	0.13 (\pm 0.06)	<u>1.52</u> (\pm 0.97)	0.58 (\pm 0.29)	<u>0.81</u> (\pm 0.47)	0.31 (\pm 0.23)	0.27 (\pm 0.25)
NIR ToF		0.10 (\pm 0.06)	0.79 (\pm 0.45)	<u>0.64</u> (\pm 0.34)	0.49 (\pm 0.21)	<u>0.84</u> (\pm 0.30)	<u>0.32</u> (\pm 0.28)
Active Stereo		0.08 (\pm 0.05)	0.18 (\pm 0.17)	0.20 (\pm 0.16)	0.13 (\pm 0.14)	0.16 (\pm 0.14)	0.16 (\pm 0.13)
Passive Stereo		<u>0.24</u> (\pm 0.11)	0.26 (\pm 0.15)	0.14 (\pm 0.11)	0.19 (\pm 0.21)	0.15 (\pm 0.11)	0.13 (\pm 0.13)
RF ToF	C_s	0.15 (\pm 0.08)	0.54 (\pm 0.40)	<u>0.97</u> (\pm 0.61)	<u>2.21</u> (\pm 2.05)	0.55 (\pm 0.77)	0.17 (\pm 0.11)
NIR ToF		0.16 (\pm 0.18)	0.79 (\pm 0.42)	0.59 (\pm 0.30)	0.53 (\pm 0.28)	1.16 (\pm 0.60)	0.43 (\pm 0.42)
Active Stereo		0.08 (\pm 0.05)	0.17 (\pm 0.15)	0.17 (\pm 0.11)	0.12 (\pm 0.38)	0.17 (\pm 0.17)	0.19 (\pm 0.76)
Passive Stereo		<u>0.30</u> (\pm 0.13)	0.33 (\pm 0.18)	0.19 (\pm 0.13)	0.23 (\pm 0.27)	0.22 (\pm 0.20)	0.18 (\pm 0.69)
RF ToF	P	0.13 (\pm 0.14)	<u>2.73</u> (\pm 2.47)	<u>1.28</u> (\pm 0.76)	<u>3.64</u> (\pm 3.23)	0.67 (\pm 1.08)	0.20 (\pm 0.26)
NIR ToF		0.19 (\pm <u>0.25</u>)	1.32 (\pm 0.58)	0.91 (\pm 0.47)	0.85 (\pm 0.52)	<u>1.57</u> (\pm 0.70)	0.77 (\pm 3.13)
Active Stereo		0.10 (\pm 0.12)	0.29 (\pm 0.42)	0.27 (\pm 0.34)	0.24 (\pm 1.25)	0.24 (\pm 0.35)	0.90 (\pm 5.17)
Passive Stereo		<u>0.36</u> (\pm 0.17)	0.47 (\pm 0.51)	0.29 (\pm 0.38)	0.35 (\pm 0.54)	0.29 (\pm 0.35)	<u>1.43</u> (\pm 7.09)
RF ToF	P_e	0.12 (\pm 0.13)	2.93 (\pm 2.60)	1.35 (\pm 0.66)	<u>3.61</u> (\pm 3.23)	0.66 (\pm 1.07)	0.20 (\pm 0.27)
NIR ToF		0.08 (\pm 0.10)	1.69 (\pm 0.23)	1.16 (\pm 0.27)	0.82 (\pm 0.38)	<u>1.70</u> (\pm 0.89)	<u>0.25</u> (\pm 0.13)
Active Stereo		0.06 (\pm 0.08)	0.42 (\pm 0.50)	0.22 (\pm 0.27)	0.16 (\pm 0.30)	0.15 (\pm 0.21)	0.16 (\pm 0.21)
Passive Stereo		<u>0.38</u> (\pm 0.14)	0.55 (\pm 0.56)	0.24 (\pm 0.29)	0.18 (\pm 0.26)	0.20 (\pm 0.22)	0.10 (\pm 0.13)

	Metric Type	S1 Hand Open	Hand Printed Flat	Mirror	Candle	Flowerpot (Transparent)	V1 Metal Plate
RF ToF	C_g	0.36 (\pm 0.38)	0.71 (\pm 0.78)	0.87 (\pm 0.26)	1.50 (\pm 1.12)	1.31 (\pm 1.21)	0.12 (\pm 0.05)
NIR ToF		0.31 (\pm 0.14)	0.25 (\pm 0.12)	<u>3.77</u> (\pm 1.97)	<u>2.04</u> (\pm 0.40)	<u>2.73</u> (\pm 1.03)	<u>0.77</u> (\pm 0.42)
Active Stereo		0.12 (\pm 0.09)	0.09 (\pm 0.07)	2.13 (\pm 1.52)	0.26 (\pm 0.29)	0.74 (\pm 0.53)	0.08 (\pm 0.06)
Passive Stereo		0.20 (\pm 0.16)	0.21 (\pm 0.37)	2.31 (\pm 1.61)	1.64 (\pm 0.78)	2.01 (\pm 0.83)	0.13 (\pm 0.07)
RF ToF	C_s	0.22 (\pm 0.15)	0.17 (\pm 0.13)	0.91 (\pm 0.14)	<u>5.57</u> (\pm 2.78)	1.86 (\pm <u>2.41</u>)	0.13 (\pm 0.06)
NIR ToF		<u>0.38</u> (\pm 0.26)	<u>0.29</u> (\pm 0.20)	<u>33.31</u> (\pm 9.07)	1.71 (\pm 0.49)	<u>3.10</u> (\pm 1.22)	<u>0.81</u> (\pm 0.43)
Active Stereo		0.13 (\pm 0.10)	0.09 (\pm 0.06)	30.21 (\pm 14.59)	0.25 (\pm 0.26)	1.27 (\pm 1.78)	0.09 (\pm 0.07)
Passive Stereo		0.26 (\pm 0.22)	0.18 (\pm <u>0.34</u>)	27.02 (\pm 11.33)	1.28 (\pm 0.65)	1.86 (\pm 0.93)	0.16 (\pm 0.11)
RF ToF	P	0.22 (\pm 0.25)	0.16 (\pm 0.20)	0.93 (\pm 0.12)	<u>7.41</u> (\pm 3.79)	2.74 (\pm <u>3.66</u>)	0.11 (\pm 0.12)
NIR ToF		<u>0.52</u> (\pm 0.43)	0.33 (\pm 0.29)	37.84 (\pm 14.84)	2.78 (\pm 0.35)	<u>5.24</u> (\pm 2.04)	<u>0.95</u> (\pm <u>0.48</u>)
Active Stereo		0.22 (\pm <u>1.25</u>)	0.16 (\pm 1.30)	<u>39.66</u> (\pm <u>24.75</u>)	0.42 (\pm 0.49)	2.08 (\pm 2.30)	0.10 (\pm 0.13)
Passive Stereo		0.35 (\pm 0.41)	<u>1.73</u> (\pm 8.95)	30.82 (\pm 14.01)	2.10 (\pm 0.98)	3.50 (\pm 1.37)	0.19 (\pm 0.15)
RF ToF	P_e	0.22 (\pm 0.25)	0.16 (\pm 0.20)	0.93 (\pm 0.12)	7.37 (\pm 3.85)	2.76 (\pm 3.66)	0.10 (\pm 0.11)
NIR ToF		<u>0.51</u> (\pm 0.27)	0.30 (\pm 0.09)	39.68 (\pm 6.57)	2.75 (\pm 0.15)	<u>6.18</u> (\pm 1.79)	<u>0.79</u> (\pm 0.39)
Active Stereo		0.16 (\pm 0.24)	0.08 (\pm 0.10)	<u>43.84</u> (\pm 20.28)	0.31 (\pm 0.44)	2.52 (\pm 1.77)	0.07 (\pm 0.09)
Passive Stereo		0.25 (\pm <u>0.34</u>)	0.17 (\pm 0.15)	35.96 (\pm 7.83)	2.15 (\pm 0.65)	4.36 (\pm 0.71)	0.15 (\pm 0.09)

Table 4. We measure the sensor-GT deviation with respect to C_g , C_s , P , and P_e , which we list in the form $(\mu \pm \sigma)$, consisting of the mean μ and standard deviation σ in centimeters, computed over the entire metric domain, respectively. The best results among all sensors of one metric type are highlighted in **bold** and the worst results are underlined. The results are discussed in Section 7.

of the 2D axis-aligned bounding box B of the antenna array by using the formula: $(A \cap B)/B$.

7 Sensor Characterization by Depth Deviation

First, we present complementary perspectives on the data, where we put the depth deviation of all 45 objects into relation with the different metric types and, subsequently, the different types of depth imagers. We analyze each representation in turn, highlighting common trends, in combination with previously stated results of Section 6.2. Finally, we examine the depth deviation obtained specifically for the selected objects of Table 4.

7.1 General Trends

Interpreting the extensive numerical data on depth deviations in Table 4 and the supplementary material can be challenging, so we provide visual, complementary views in this section. In order to relate different quantities to each other, we use barycentric interpolation based on triples of metric types (Figure 7) and sensors (Figure 8), respectively. For each triple (μ_a, μ_b, μ_c) , the mean values for depth deviation (μ) of each object are transformed to affine coordinates (w_a, w_b, w_c) by using the formula $w_{\{a,b,c\}} = \mu_{\{a,b,c\}} / (\mu_a + \mu_b + \mu_c)$. Circle locations closer to a triangle corner indicate higher relative depth deviation. Moreover, as the triples are drawn from a set of

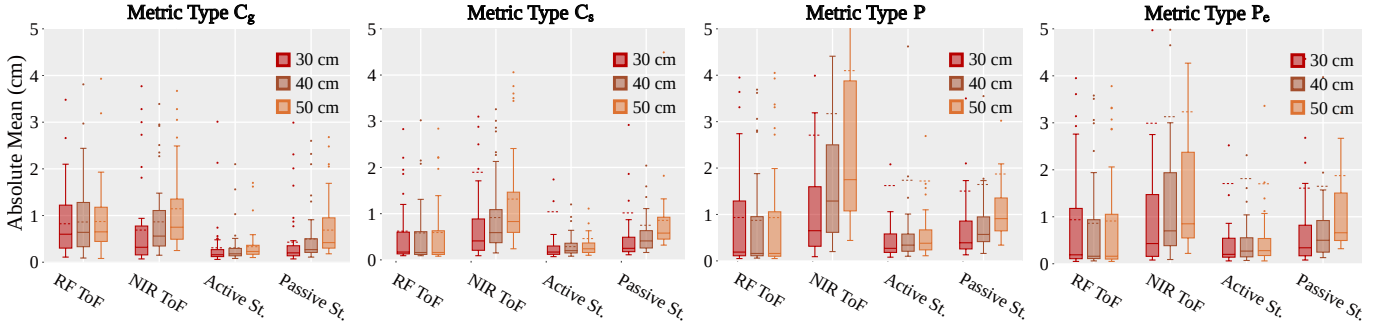


Fig. 5. We plot the distribution of the mean error across all objects with respect to different object-to-sensor distances. Solid (—) and dashed (---) horizontal lines indicate the median and the mean of the distribution, respectively. The results are discussed in Section 7.

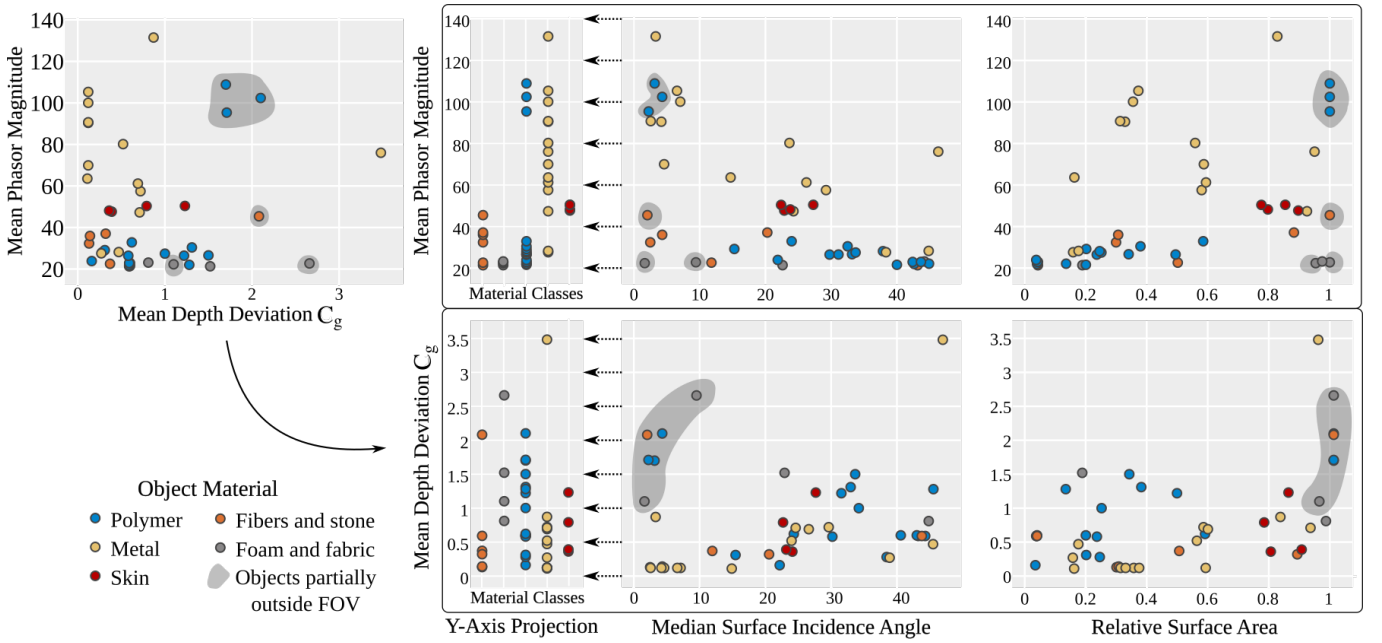


Fig. 6. We present the received signal magnitude (mean absolute phasor value) in relation to the mean depth deviation of metric C_g and further investigate both quantities with respect to varying object material, geometry (median surface incidence angle), and size (relative surface area). We highlight measurements where large objects appear outside the radar’s field of view (FOV) in grey regions, as they exhibit comparatively higher depth deviations compared to the ground truth reconstructions that possibly extend beyond this FOV. The results are discussed in Section 9.

four, the triangles are arranged in the shape of an unfolded tetrahedron, highlighting that each triangle’s contents can be seen as a projection of barycentric coordinates within a (3D) tetrahedron $w_{\{a,b,c,d\}} = w_{\{a,b,c,d\}} / (w_a + \dots + w_d)$.

In Figure 7, we provide a qualitative comparison of each sensor’s depth deviation from GT with respect to the four presented metrics. In dense reconstructions, as is typical for optical depth sensors, metrics based on nearest neighbors (here, C_g and C_s) are bound to be lower than those based on projection (P and P_e); they also tend to be more resilient against noise. For RF reconstructions, however, that are prone to sparse depth maps, Chamfer distances often create false matches; accordingly, C_g dominates for RF ToF compared to

the other metrics. For further discussion regarding the sparsity of RF reconstructions, see Section 9.

For optical sensors, a marginal trend towards the corners of C_s and P , away from the silhouette-resilient P_e and C_g , cf. Table 3, indicates the presence of noise at object silhouettes.

In Figure 8, we observe a considerable spread of depth deviations across different sensors. As noted in Section 6.2, the relative depth deviation between sensors ranges from 1.9 to 3.4 mm, that is, the variation in the depicted normalized error occurs within a comparatively small range of absolute errors. As a general trend, the two stereo sensors have the lowest depth deviation (see triangles N–R–A and N–R–W), with a moderate edge for active stereo,

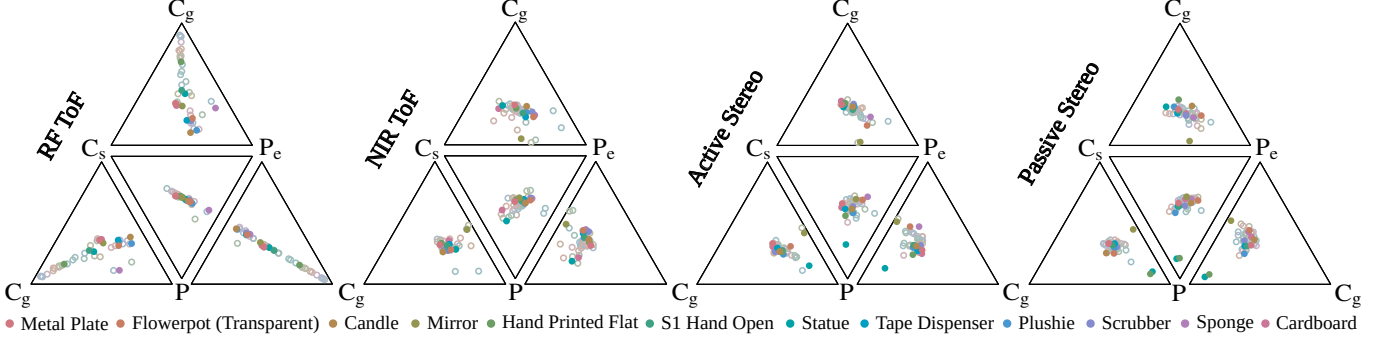


Fig. 7. A complementary view on the depth deviation across different *metric types*. For each triplet of metrics $M_i \in \{C_g, C_s, P, P_e\}$, we convert each mean depth deviation μ_i to affine coordinates, $\bar{\mu}_i = \mu_i / \sum_i \mu_i$, that map an object’s errors in to a triangle whose corners correspond to metrics M_i . All 45 MAROON objects are shown as circles, with selected objects from Table 4 highlighted in solid colors. Samples closer to a triangle corner indicate a higher relative depth deviation in the corresponding metric.

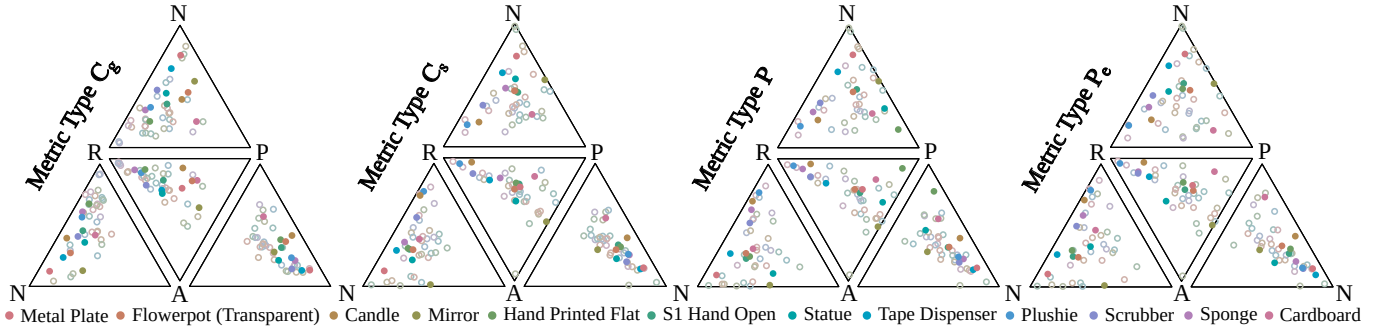


Fig. 8. A complementary view on the depth deviation across different *sensors*. The sensors are denoted as **R** (RF ToF), **N** (NIR ToF), **A** (Active Stereo), and **P** (Passive Stereo), respectively. Analogously to Figure 7, we convert the mean depth deviations μ_i to affine coordinates within triangles corresponding to all possible sensor triples. All 45 MAROON objects are shown as circles, with selected objects from Table 4 highlighted in solid colors. Samples closer to a triangle corner indicate a higher relative depth deviation for the corresponding sensor.

particularly for metrics P and P_e , see the A – P axis, where passive stereo’s performance degrades. This is consistent with the results in Section 6.2.1, where we find that the active stereo has the highest number of best results. However, given that relative depth deviations between sensors differ by only a few millimeters, we conclude that the seemingly improved depth quality of active stereo sensors is of minimal significance. Moreover, an examination of the scatter plot reveals a marginal weight trend towards the corners of the two ToF sensors. Reconstruction errors between the two ToF sensors are highly object-dependent, and many objects, including many of the highlighted ones, demonstrate multi-path effects due to perfect signal reflections, retro-reflectivity, or partial signal transmission. Further details on this will be discussed in the next section.

Considering the results over varying object-to-sensor distances in Figure 5, we observe that the depth deviation of the passive stereo and the NIR ToF sensor is significantly more distance-specific compared to active stereo and RF ToF. For passive stereo, this may be due to a decrease in effective spatial resolution, where δ_z directly depends on $\delta_{x,y}$ (see supplementary). As the distance between the object and the sensor increases, $\delta_{x,y}$ decreases, resulting in a loss of high-frequency color details while the object appears smaller in

the image. Compared to passive stereo, the active stereo sensor has a comparably higher effective resolution, assuming that the resolution of both sensors differs in accordance with δ_{xyz} in Table 1. The unique active NIR pattern may also be less sensitive to decreases in spatial resolution, maintaining the quality of correspondence matches. The trend for the NIR ToF sensor aligns with findings from Bamji et al. [2018] for 30–50 cm distances. However, we argue that absolute errors for a target with 20% reflectivity do not fully represent all objects in our experiments. We suggest that, in addition to the expected decrease in spatial resolution, a greater depth deviation with increasing distance arises from the signal-to-noise ratio with respect to environmental light, which typically decreases over distance due to the inverse-square law.

Notably, in our results, RF ToF does not exhibit a distance-dependent depth deviation, unlike its optical counterpart. This seems to contradict Table 1, where δ_z for RF ToF degrades more rapidly with depth, compared to optical sensors; however, the theoretical decay with depth stems from the worsening separability of neighboring point targets, which is not a pertinent scenario in our database, as the recorded targets primarily have smooth surfaces at locations where valid reconstructions are measured. Moreover, our setup

minimizes mmWave interactions with external objects, limiting noise primarily to the object itself. As a result, the signal-to-noise ratio of RF ToF is considerably less sensitive to changes in object-to-sensor distance compared to NIR ToF, assuming no interference from external sources.

7.2 Object-specific Observations

The following section will analyze the objects in Table 4 in regard to their relative depth deviations over one or multiple sensors. For RF ToF, we find that the least deviation relative to the mean of all metrics occurs with planar object geometries (*V1 Metal Plate*, *Cardboard*), followed by more complex shapes (*Statue*, *S1 Hand Open*, *Hand Printed Flat*). For a deeper discussion, see Section 9.

Objects made of foam (*Sponge*), thin plastic (*Scrubber*, *Flowerpot*), fabric (*Plushie*), and paraffin wax (*Candle*), exhibit the highest depth deviations due to a large fraction of the transmitted RF signal not being immediately reflected. In the case of *Mirror*, RF penetrates the first (glass) surface and images the silver coating behind, leading to an offset in the depth reconstruction.

For similar reasons, NIR ToF shows large depth deviations for visually transparent objects like *Flowerpot*, *Candle*, *Sponge*, and *Tape Dispenser*. Although both RF ToF and NIR ToF are susceptible to multi-path effects, our experiments suggest these effects do not occur for the same objects. Further examination of wavelength-specific multi-path effects, with a particular focus on partially transmissive materials, will be discussed in Section 8.

Additional sources of high depth deviation for NIR ToF include thin structures (*Scrubber*), which reduce the sensor’s effective spatial resolution. Highly reflective objects (*Metal Plate*) may cause sensor oversaturation, while perfectly specular materials (*Mirror*) yield depth values not from the object’s surface but from the first weak scatterer encountered along the reflection path.

For the active stereo sensor, we observe higher depth deviations for textureless and partially transmissive materials (*Sponge*, *Candle*). Similar to NIR ToF, the uniqueness of the active NIR light pattern can be compromised by multi-path effects. Finally, as expected, the passive stereo camera is particularly sensitive to textureless objects (*Sponge*, *Candle*).

8 Discussion ToF in Partially Transmissive Media

As previously discussed in Section 4.2.2, both NIR and RF ToF sensors assume direct reflection and thus are susceptible to internal reflections, such that multi-path effects within the scene may lead to missing or incorrect reconstructions. In this analysis, following the nomenclature by Nayar et al. [2006], we classify radiance transport that involves a single signal bounce between sender and receiver as *direct* (as, within the sensor’s spatial resolution, it interacts with the scene at one surface point only), and all other types of transport as *global* (involving multiple scattering or diffraction events within and between objects). Due to their significant difference in wavelength relative to scene features, global radiance transport takes very different forms for each modality. In the case of NIR, representative forms of global transport include inter-reflections, half-transparent surfaces, and subsurface scattering within the object material. Global transport at radio frequencies, on the other

hand, is dominated by diffraction and reflections that reshape and redirect the wave front as it interacts with multiple scene elements, and by multiple superimposed responses akin partial transmittance at different depths.

In the remainder, we will now study four selected objects, shown in Figure 9. In addition to Table 4, this figure visualizes depth reconstruction deviations using a signed version P^* of our metric P , color-encoded on a symmetrical logarithmic scale (SymLogNorm^2), with a linear mapping between $[-0.5, 0.5]$ centimeters. The supplementary material includes signed versions of P and P_e for all MAROON objects.

In the NIR domain, the most prominent effect of global transport occurs for objects with strong internal scattering. Here, the ToF reconstructions exhibit systematic depth deviations of P^* , generally biased toward larger distances than the ground truth. This is consistent with the light traveling an additional distance due to scattering within the object before being remitted again, so that the observed propagation time of the actively transmitted signal is consistently longer than for a direct (local) reflection at the object surface. Examples in Figure 9 for internal scattering include *subsurface scattering* (*S1 Hand Open*, *Sponge*, *Candle*) and *inter-reflections* within hollow objects (*Tape Dispenser*). Extended path length due to subsurface scattering is an established effect, systematically measured by Lukinsone et al. [2020]. For human skin (as in our dataset *S1 Hand Open*), and for points of incidence and exitance one millimeter apart, Lukinsone et al. observe effective sub-surface path lengths of up to 26 ± 3 mm at 800 nm wavelength, which — in the context of a ToF sensor — would result in a systematic depth deviation of half that path length ($\approx +13$ mm). At the same time, however, for human skin a significant portion of the total remitted light stays very close to the point of incidence [Jensen et al. 2001], suggesting that the bulk of the received signal experiences even smaller path length extensions, lending plausibility to our measured systematic depth deviation of $+4.9$ mm for *S1 Hand Open* to be due to subsurface scattering.

For RF ToF, only one object (*Candle*) showed a systematic path length extension, suggesting that optical subsurface scattering cannot fully model RF interactions. In contrast to the NIR ToF measurements, the depth deviation for the *Candle* object is non-uniform, with higher values near the edges due to variations in surface position and orientation that affect radiance transport.

Where the *Candle* surface faces the antenna array, the received signal is dominated by direct reflections; where direct reflections reflect away from the array (nearer to the candle’s silhouettes), mostly global transport is observed. In accordance with the results by Álvarez López et al. [2018] the depth reconstruction in the parts with little direct reflection appear more distant than ground truth, which the authors attribute to the high relative permittivity $\epsilon_r \approx 2.6$ of paraffin wax that extends the inferred path length under the assumption of speed of light in vacuum.

In summary, objects composed of partially transmissive media primarily yield systematic bias in ToF reconstructions, with estimated depths biased toward larger values than the ground truth.

²https://matplotlib.org/3.8.4/api/_as_gen/matplotlib.colors.SymLogNorm.html

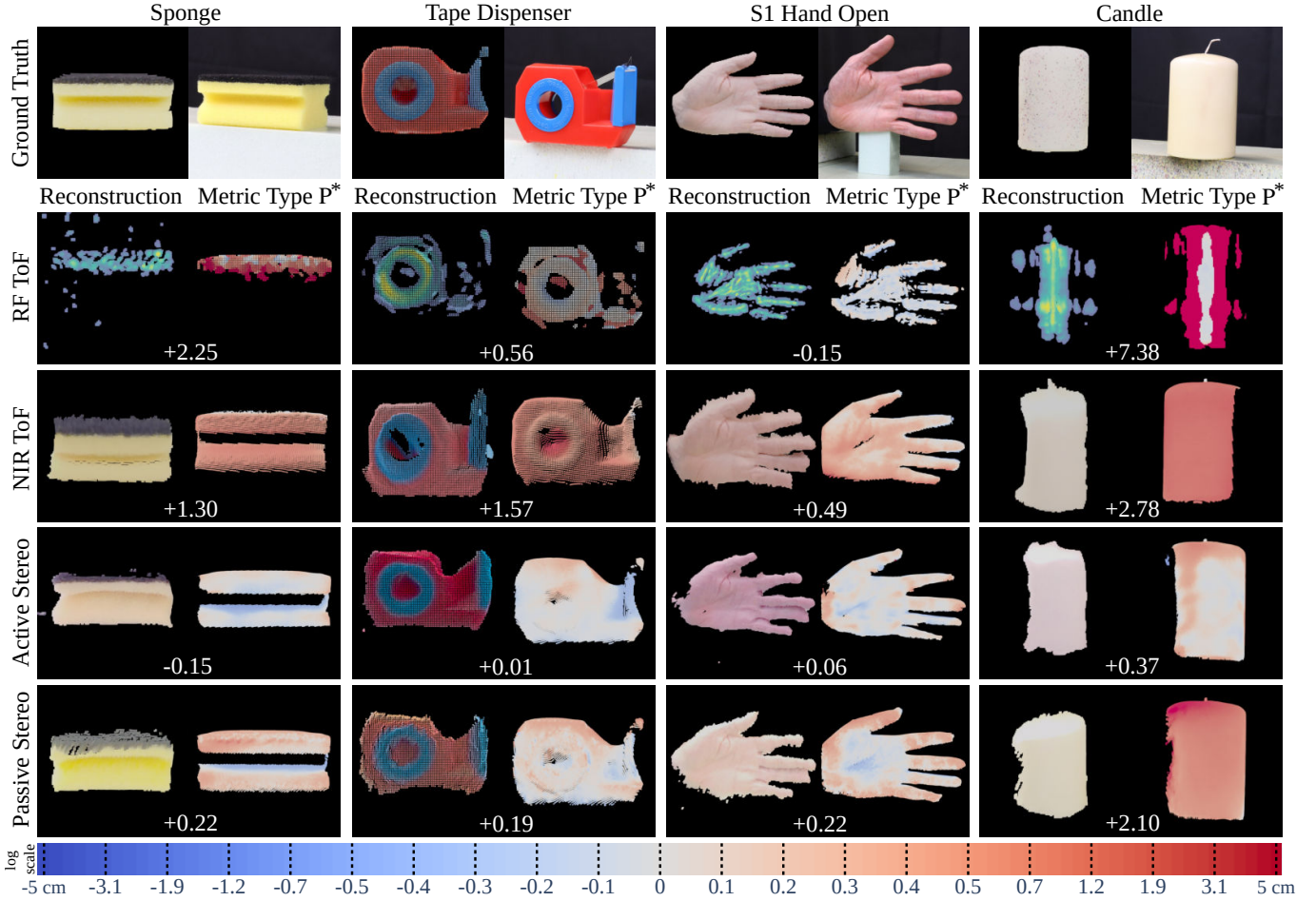


Fig. 9. For selected objects, we show the reconstructed pointclouds (*left*) next to their deviation from to the MVS reconstruction (*right*). The signed depth deviation P^* is given for each pixel (u, v) in centimeters. All measurements in the domain $M^+(u, v)$ are projected onto the GT reconstruction and mapped to color using a combination of a symmetrical logarithmic scale and linear mapping between $[-0.5, 0.5]$. Furthermore, we quantify the mean deviation of P^* in centimeters below each sensor measurement.

Nevertheless, the factors causing these distortions vary between optical and RF modalities.

9 Discussion of MIMO Radar Signal and Reconstruction

Our observations in Section 7 suggest that RF ToF reconstructions are generally less complete than those of optical sensors, as illustrated in the *second* row of Figure 9, where quality is best when surface orientations align with the antenna aperture. To identify sources of incomplete RF ToF reconstructions, we first analyze the raw signal response — without inducing additional bias from the reconstruction algorithms — and subsequently relate it to the quality of the measured depth after reconstruction.

In Figure 6, we presented the received signal magnitude across objects with varying material, geometry (surface incidence angle) and size (relative surface area). Following the scatter plot order from left to right, we will now discuss common trends, noting that it remains challenging to disentangle the presented quantities, as

the large variability across objects prevents us from isolating one quantity while keeping the others constant. Further results where we discuss the potential relation between object size and object geometry are given in the supplementary material.

Considering *object material*, metal and metallic-coated objects generally show higher signal magnitudes, which is consistent with previous studies [Ahmed 2014, 2021]. With a considerably lower spread, large magnitudes are also observed for captures of human skin, which is highly reflective due to its rich water content [Ahmed 2014]. Object materials made of polymers, fibers and stone, or foam generally respond with much smaller signal magnitude.

Regarding *object geometry* and *size*, no significant global trends are observed; however, consistent patterns emerge within subsets of the same material, particularly in the metal and polymer classes, which have the highest number of samples. For objects of more complex *geometry*, with a median surface incidence angle greater than 10° , large portions of their surface area face away from the

antenna array, resulting in decreased signal responses compared to planar objects aligned closely with the antenna aperture ($<10^\circ$). The reflection direction of the transmitted signal depends on the surface normal's orientation. As the angle between this normal and the depth axis increases, the solid angle of the object relative to the planar square-shaped antenna aperture (cf. Table 1) decreases. In other words, a decreasing area around the hemisphere of outgoing reflection directions is aligned with the 65° field of view of the RX antennas, resulting in reduced signal energy reception, and thus radar cross-section [Knott et al. 2004]. Superficially this resembles the well-known cosine law in radiometry, but the exact quantitative relationship depends on the object's location relative to the individual RX and TX antennas and is further modulated by the non-trivial radiation and signal lobes of the antennas.

Aside from object geometry, the received signal magnitude also appears to increase with *object size* for non-metal materials. Within these material classes, the highest signal magnitude is achieved for objects close to or even larger (objects partially outside FOV) than the antenna aperture. As the latter also typically exhibits a low median surface incidence angle, it remains questionable, whether this observation can be attributed to object size or object geometry. To address this, we additionally visualize the relation between the two quantities in the supplementary material. Assuming that signal magnitude is proportional to the received energy, our findings correspond to the fact that, the reflected signal energy received at the RX antennas directly depends on the surface area of the irradiated object, in case the energy density is constant. To summarize, we identified object geometry and material as two factors that influence the maximum signal magnitude at each receiver, while also observing indications of the relevance of object size.

We now continue to investigate the relationship between signal magnitude and the observed depth deviation, which is illustrated in the *upper left* scatter plot in Figure 6. Focusing on polymer and metal objects, we generally find no direct relationship between signal magnitude and depth deviation. Polymer and metal objects have a large spread in the x - and y -axis, respectively, while the opposite axis has comparably low variation. The received signal magnitude may have a more significant influence on the reconstruction quality in less constrained scenarios, involving multiple objects and signal sources, where, for example, depth filtering becomes increasingly relevant. In our experiments, within the RF near field, we suggest that reconstruction quality is more closely related to the distribution of received signals across antennas, influenced primarily by the local antenna layout and characteristics.

Having found no direct relation between signal magnitude and the reconstruction quality, we now examine the *depth deviation* concerning the previously mentioned three object quantities, which are shown in the bottom row of Figure 6. Similar to our findings for signal magnitude, metal objects generally exhibit the lowest depth deviation with a relatively small spread compared to other material classes, indicating that *object material* influences reconstruction quality. Furthermore, we find no direct relationship between *object size* and reconstruction quality. The most notable trend is seen with varying *object geometry*, where depth error increases alongside the median surface incidence angle across all material classes. The backprojection algorithm assumes that similar energy amounts are

received at a point across the majority of RX antennas. Received energy diminishes for surfaces oriented away from the antenna geometry, leading to variations based on antenna positioning. This, in turn, can lead to reduced confidence in the measurements, causing valid data to be filtered out along with noise.

To conclude, the analysis of MIMO imaging radar reconstructions based on the received signal response is considerably less straightforward than that of optical sensors. Our findings suggest that the reconstruction quality of RF ToF sensors is primarily influenced by object geometry, followed by the influence of object material, especially in depth filtering with respect to signal confidence.

9.1 Limitations

Even though the depth deviation of the MIMO imaging radar is on par with that of optical sensors, the reconstructions exhibit significantly more holes, where no valid depth is estimated. While it is intuitive to assume that reconstruction quality is influenced by object material (limiting the returned signal amount — akin to optically transmissive materials), we observe that in our experiments the object geometry is the primary factor of influence and has a greater impact than in optical sensors; however, disentangling the effects of geometry and material remains challenging, as precise impacts on fine-grained surface details cannot be easily assessed. Without a direct mapping between point targets and RX antennas, depth evaluation concerning these surface-level details is infeasible without backprojection. On the other hand, the reconstructed outcomes of backprojection may not align with reality, as the method incorporates a systematic bias by relying on the Born approximation [Ahmed 2014]. To overcome these limitations, we suggest using simulation frameworks, such as employed by Schuessler et al. [2021] or Bräunig et al. [2023a]. These could help disentangle potential error sources behind missing reconstructions and enhance the current signal processing methods.

Furthermore, it should be noted that the object reconstructions were evaluated solely for valid locations in the ground-truth data, excluding artifacts like ghost targets or other forms of noise that may arise from violations of the Born approximation. Lastly, we did not capture different orientations of flat objects, which would be an interesting future direction to investigate object orientation in isolation from geometry complexity.

10 Conclusion

In this paper, we present a novel multimodal dataset, MAROON, that allows us to characterize, for the first time, near-field MIMO imaging radars in direct relation with traditional depth imagers from the optical frequency domain for close-range applications. The dataset comprises depth images of a variety of objects, synchronously captured by four mutually calibrated depth imagers and a ground-truth multi-view stereo system. We subsequently analyzed the data within a comprehensive evaluation framework, offering quantitative and qualitative perspectives on each sensor's depth deviation across multiple metric types, objects, and object-to-sensor distances.

In summary, our analysis revealed the following insights:

- There is no single sensor modality that would consistently outperform the others. Each sensor has unique strengths and weaknesses related to the object's material, geometry, and distance from the sensor.
- NIR ToF displays systematic depth distortions due to effects of global radiance transport within partially transmissive media, whereas RF ToF reconstructions were mostly unaffected.
- RF ToF partially exhibits missing reconstructions compared to its optical counterpart, primarily due to the object geometry contributing to the reconstruction sparseness.

We hope that the public release of the MAROON dataset will give rise to further study of multimodal sensors in a joint reference frame. The findings presented here are based on aggregate trends and individual object analyses that contribute to the understanding of the addressed sensor characteristics; however, we believe that our dataset still invites further analysis, exploiting the high diversity of the 45 objects that could not be fully addressed in the scope of this paper. Furthermore, we anticipate that insights into the complementary strengths of optical and near-field radio-frequency depth imagers will benefit future sensor fusion applications.

Acknowledgement

The authors would like to thank the Rohde & Schwarz GmbH & Co. KG (Munich, Germany) for providing the radar imaging devices.

This work was funded by the Deutsche Forschungsgemeinschaft (DFG, German Research Foundation) – SFB 1483 – Project-ID 442419336, EmpkinS.

The authors gratefully acknowledge the scientific support and HPC resources provided by the Erlangen National High Performance Computing Center of the Friedrich-Alexander-Universität Erlangen-Nürnberg.

References

- Sherif Sayed Ahmed. 2014. *Electronic Microwave Imaging with Planar Multistatic Arrays*. Logos Verlag, DEU.
- Sherif Sayed Ahmed. 2021. Microwave Imaging in Security – Two Decades of Innovation. *IEEE Journal of Microwaves* 1, 1 (2021), 191–201. <https://doi.org/10.1109/JMW.2020.3035790>
- Cyrus S. Bamji, Swati Mehta, Barry Thompson, Tamer Elkhatab, Stefan Wurster, Onur Akkaya, Andrew Payne, John Godbaz, Mike Fenton, Vijay Rajasekaran, Larry Prather, Satya Nagaraja, Vishali Mogallapu, Dane Snow, Rich McCauley, Mustansir Mukadam, Iskender Agi, Shaun McCarthy, Zhanping Xu, Travis Perry, William Qian, Vei-Han Chan, Prabhu Adepur, Gazi Ali, Muneeb Ahmed, Aditya Mukherjee, Sheethal Nayak, Dave Gampell, Sunil Acharya, Lou Kordus, and Pat O'Connor. 2018. IMpixel 65nm BSI 320MHz demodulated TOF Image sensor with 3 μ m global shutter pixels and analog binning. In *2018 IEEE International Solid-State Circuits Conference - (ISSCC)*. 94–96. <https://doi.org/10.1109/ISSCC.2018.8310200>
- Akanksha Bhutani, Sören Marahrens, Marius Kretschmann, Serdal Ayhan, Steffen Scherr, Benjamin Göttel, Mario Pauli, and Thomas Zwick. 2022. Applications of radar measurement technology using 24 GHz, 61 GHz, 80 GHz and 122 GHz FMCW radar sensors. *Technisches Messen* 89, 2 (2022), 107–121. <https://doi.org/doi:10.1515/teme-2021-0034>
- DW Bliss and KW Forsythe. 2003. Multiple-input multiple-output (MIMO) radar and imaging: degrees of freedom and resolution. In *The Thrity-Seventh Asilomar Conference on Signals, Systems & Computers, 2003*, Vol. 1. IEEE, 54–59.
- Johanna Braeunig, Desai Mejdani, Daniel Krauss, Stefan Griesshammer, Robert Richer, Christian Schuessler, Julia Yip, Tobias Steigleder, Christoph Ostgathe, Bjoern M. Eskofier, and Martin Vossiek. 2023. Radar-based Recognition of Activities of Daily Living in the Palliative Care Context Using Deep Learning. In *2023 IEEE EMBS International Conference on Biomedical and Health Informatics (BHI)*. 1–4. <https://doi.org/10.1109/BHI58575.2023.10313506>
- Johanna Bräunig, Christian Schüller, Vanessa Wirth, Marc Stamminger, Ingrid Ullmann, and Martin Vossiek. 2023a. A Realistic Radar Ray Tracing Simulator for Hand Pose Imaging. [arXiv:2307.15412](https://arxiv.org/abs/2307.15412) <https://arxiv.org/abs/2307.15412>
- Johanna Bräunig, Vanessa Wirth, Christoph Kammel, Christian Schüller, Ingrid Ullmann, Marc Stamminger, and Martin Vossiek. 2023b. An Ultra-Efficient Approach for High-Resolution MIMO Radar Imaging of Human Hand Poses. *IEEE Transactions on Radar Systems* 1 (2023), 468–480. <https://doi.org/10.1109/TRS.2023.3309574>
- Anjun Chen, Xiangyu Wang, Kun Shi, Shaohao Zhu, Bin Fang, Yingfeng Chen, Jiming Chen, Yuchi Huo, and Qi Ye. 2023. ImmFusion: Robust mmWave-RGB Fusion for 3D Human Body Reconstruction in All Weather Conditions. In *2023 IEEE International Conference on Robotics and Automation (ICRA)*. 2752–2758. <https://doi.org/10.1109/ICRA48891.2023.10161428>
- Anjun Chen, Xiangyu Wang, Shaohao Zhu, Yanxu Li, Jiming Chen, and Qi Ye. 2022. MmBody Benchmark: 3D Body Reconstruction Dataset and Analysis for Millimeter Wave Radar. In *Proceedings of the 30th ACM International Conference on Multimedia (Lisboa, Portugal) (MM '22)*. Association for Computing Machinery, New York, NY, USA, 3501–3510. <https://doi.org/10.1145/3503161.3548262>
- Chuang-Yuan Chiu, Michael Thelwell, Terry Senior, Simon Choppin, John Hart, and Jon Wheat. 2019. Comparison of depth cameras for three-dimensional reconstruction in medicine. *Proceedings of the Institution of Mechanical Engineers, Part H: Journal of Engineering in Medicine* 233, 9 (2019), 938–947. <https://doi.org/10.1177/0954411919859922> [arXiv:https://doi.org/10.1177/0954411919859922](https://doi.org/10.1177/0954411919859922) PMID: 31250706
- Yoshana Deep, Patrick Held, Shobha Sundar Ram, Dagmar Steinhäuser, Anshu Gupta, Frank Gruson, Andreas Koch, and Anirban Roy. 2020. Radar cross-sections of pedestrians at automotive radar frequencies using ray tracing and point scatterer modelling. *IET Radar, Sonar & Navigation* 14, 6 (2020), 833–844. <https://doi.org/10.1049/iet-rsn.2019.0471> [arXiv:https://ietresearch.onlinelibrary.wiley.com/doi/pdf/10.1049/iet-rsn.2019.0471](https://doi.org/10.1049/iet-rsn.2019.0471)
- Silvio Giancola, Matteo Valenti, and Remo Sala. 2018. *A Survey on 3D Cameras: Metrological Comparison of Time-of-Flight, Structured-Light and Active Stereoscopic Technologies* (1st ed.). Springer Publishing Company, Incorporated.

- Georg Halmetschlager-Funek, Markus Suchi, Martin Kampel, and Markus Vincze. 2019. An Empirical Evaluation of Ten Depth Cameras: Bias, Precision, Lateral Noise, Different Lighting Conditions and Materials, and Multiple Sensor Setups in Indoor Environments. *IEEE Robotics & Automation Magazine* 26, 1 (2019), 67–77. <https://doi.org/10.1109/MRA.2018.2852795>
- Miles Hansard, Seungkyu Lee, Ouk Choi, and Radu Horaud. 2012. *Time-of-Flight Cameras: Principles, Methods and Applications*. Springer Publishing Company, Incorporated.
- Jürgen Hasch, Eray Topak, Raik Schnabel, Thomas Zwick, Robert Weigel, and Christian Waldschmidt. 2012. Millimeter-Wave Technology for Automotive Radar Sensors in the 77 GHz Frequency Band. *IEEE Transactions on Microwave Theory and Techniques* 60, 3 (2012), 845–860. <https://doi.org/10.1109/TMTT.2011.2178427>
- Intel 2023. *Intel® RealSense™ Product Family D400 Series*. Intel. <https://www.intelrealsense.com/download/21345/?tmstsv=1697035582>
- Henrik Wann Jensen, Stephen R. Marschner, Marc Levoy, and Pat Hanrahan. 2001. A practical model for subsurface light transport. In *Proceedings of the 28th Annual Conference on Computer Graphics and Interactive Techniques (SIGGRAPH '01)*. Association for Computing Machinery, New York, NY, USA, 511–518. <https://doi.org/10.1145/383259.383319>
- Uma S. Jha. 2018. The millimeter Wave (mmW) radar characterization, testing, verification challenges and opportunities. In *2018 IEEE AUTOTESTCON*. 1–5. <https://doi.org/10.1109/AUTEST.2018.8532561>
- E.F. Knott, J.F. Schaeffer, and M.T. Tully. 2004. *Radar Cross Section*. Institution of Engineering and Technology. <https://books.google.de/books?id=0WuGjb8sqCUC>
- Shih-Po Lee, Niraj Prakash Kini, Wen-Hsiao Peng, Ching-Wen Ma, and Jenq-Neng Hwang. 2023. HuPR: A Benchmark for Human Pose Estimation Using Millimeter Wave Radar. In *2023 IEEE/CVF Winter Conference on Applications of Computer Vision (WACV)*. 5704–5713. <https://doi.org/10.1109/WACV56688.2023.00567>
- Jaime Lien, Nicholas Gillian, M. Emre Karagozler, Patrick Amihoud, Carsten Schwesig, Erik Olson, Hakim Raja, and Ivan Poupyrev. 2016. Soli: ubiquitous gesture sensing with millimeter wave radar. *ACM Trans. Graph.* 35, 4, Article 142 (jul 2016), 19 pages. <https://doi.org/10.1145/2897824.2925953>
- Teck-Yian Lim, Spencer A. Markowitz, and Minh N. Do. 2021. RaDiCaL: A Synchronized FMCW Radar, Depth, IMU and RGB Camera Data Dataset With Low-Level FMCW Radar Signals. *IEEE Journal of Selected Topics in Signal Processing* 15, 4 (2021), 941–953. <https://doi.org/10.1109/JSTSP.2021.3061270>
- Alvaro Lopez Paredes, Qiang Song, and Miguel Heredia Conde. 2023. Performance Evaluation of State-of-the-Art High-Resolution Time-of-Flight Cameras. *IEEE Sensors Journal* 23, 12 (2023), 13711–13727. <https://doi.org/10.1109/JSEN.2023.3273165>
- Vanesa Lukinsone, Anna Maslobojeva, Uldis Rubins, Maris Kuzminskis, M. Osis, and Janis Spigulis. 2020. Remitted photon path lengths in human skin: in-vivo measurement data. *Biomedical Optics Express* 11 (05 2020). <https://doi.org/10.1364/BOE.388349>
- Emidio Marchetti, Rui Du, Ben Willetts, Fatemeh Norouzian, Edward G. Hoare, Thuy Yung Tran, Nigel Clarke, Mikhail Cherniakov, and Marina Gashinova. 2018. Radar cross-section of pedestrians in the low-THz band. *IET Radar, Sonar & Navigation* 12, 10 (2018), 1104–1113. <https://doi.org/10.1049/iet-rsn.2018.5016> arXiv:https://ietresearch.onlinelibrary.wiley.com/doi/pdf/10.1049/iet-rsn.2018.5016
- Microsoft 2022. *Azure Kinect DK hardware specifications*. Microsoft. <https://learn.microsoft.com/en-us/azure/kinect-dk/hardware-specification>
- Shree K. Nayar, Gurunandan Krishnan, Michael D. Grossberg, and Ramesh Raskar. 2006. Fast separation of direct and global components of a scene using high frequency illumination (SIGGRAPH '06). Association for Computing Machinery, New York, NY, USA, 935–944. <https://doi.org/10.1145/1179352.1141977>
- Tianhe Ren, Shilong Liu, Ailing Zeng, Jing Lin, Kunchang Li, He Cao, Jiayu Chen, Xinyu Huang, Yukang Chen, Feng Yan, Zhaoyang Zeng, Hao Zhang, Feng Li, Jie Yang, Hongyang Li, Qing Jiang, and Lei Zhang. 2024. Grounded SAM: Assembling Open-World Models for Diverse Visual Tasks. arXiv:cs.CV/2401.14159
- Rohde & Schwarz 2023. *R&S® QAR50 Quality automotive radome tester*. Rohde & Schwarz. https://www.rohde-schwarz.com/products/test-and-measurement/radome-tester/rs-qar50-quality-automotive-radome-tester_63493-1138625.html?change_c=true
- Dominik Schwarz, Nico Riese, Ines Dorsch, and Christian Waldschmidt. 2022. System Performance of a 79 GHz High-Resolution 4D Imaging MIMO Radar With 1728 Virtual Channels. *IEEE Journal of Microwaves* 2, 4 (2022), 637–647. <https://doi.org/10.1109/JMW.2022.3196454>
- Christian Schüssler, Marcel Hoffmann, Johanna Bräunig, Ingrid Ullmann, Randolph Ebel, and Martin Vossiek. 2021. A Realistic Radar Ray Tracing Simulator for Large MIMO-Arrays in Automotive Environments. *IEEE Journal of Microwaves* 1, 4 (2021), 962–974. <https://doi.org/10.1109/JMW.2021.3104722>
- Krishnasamy T. Selvan and Ramakrishna Janaswamy. 2017. Fraunhofer and Fresnel Distances: Unified derivation for aperture antennas. *IEEE Antennas and Propagation Magazine* 59, 4 (2017), 12–15. <https://doi.org/10.1109/MAP.2017.2706648>
- Vasilii Semkin, Jaakko Haarla, Thomas Pairon, Christopher Slezak, Sundee Rangan, Ville Viikari, and Claude Oestges. 2020. Analyzing Radar Cross Section Signatures of Diverse Drone Models at mmWave Frequencies. *IEEE Access* 8 (2020), 48958–48969. <https://doi.org/10.1109/ACCESS.2020.2979339>
- Stereolabs 2023. *ZED X Datasheet*. Stereolabs. <https://cdn2.stereolabs.com/assets/datasheets/zed-x-datasheet-march-2023.pdf>
- Shunqiao Sun, Athina P. Petropulu, and H. Vincent Poor. 2020. MIMO Radar for Advanced Driver-Assistance Systems and Autonomous Driving: Advantages and Challenges. *IEEE Signal Processing Magazine* 37, 4 (2020), 98–117. <https://doi.org/10.1109/MSP.2020.2978507>
- Richard Szeliski. 2022. *Computer Vision - Algorithms and Applications, Second Edition*. Springer. 749–797 pages. <https://doi.org/10.1007/978-3-030-34372-9>
- Klen Čopić Pucihar, Nuwan T. Attygalle, Matjaz Kljun, Christian Sandor, and Luis A. Leiva. 2022. Solids on Soli: Millimetre-Wave Radar Sensing through Materials. *Proc. ACM Hum.-Comput. Interact.* 6, EICS, Article 156 (jun 2022), 19 pages. <https://doi.org/10.1145/3532212>
- Gustavo Velasco-Hernandez, De Jong Yeong, John Barry, and Joseph Walsh. 2020. Autonomous Driving Architectures, Perception and Data Fusion: A Review. In *2020 IEEE 16th International Conference on Intelligent Computer Communication and Processing (ICCP)*. 315–321. <https://doi.org/10.1109/ICCP51029.2020.9266268>
- Alexander Vilesov, Pradyumna Chari, Adnan Armouti, Anirudh Bindiganavale Harish, Kimaya Kulkarni, Ananya Deoghare, Laleh Jalilian, and Achuta Kadambi. 2022. Blending camera and 77 GHz radar sensing for equitable, robust plethysmography. *ACM Trans. Graph.* 41, 4, Article 36 (jul 2022), 14 pages. <https://doi.org/10.1145/3528223.3530161>
- Te-Mei Wang and Zen-Chung Shih. 2021. Measurement and Analysis of Depth Resolution Using Active Stereo Cameras. *IEEE Sensors Journal* 21, 7 (2021), 9218–9230. <https://doi.org/10.1109/JSEN.2021.3054820>
- Shunjun Wei, Zichen Zhou, Mou Wang, Jinshan Wei, Shan Liu, Jun Shi, Xiaoling Zhang, and Fan Fan. 2021. 3DRIED: A High-Resolution 3-D Millimeter-Wave Radar Dataset Dedicated to Imaging and Evaluation. *Remote Sensing* 13, 17 (2021). <https://doi.org/10.3390/rs13173366>
- C.S. Williams and O.A. Becklund. 2002. *Introduction to the Optical Transfer Function*. SPIE Press. <https://books.google.de/books?id=b5tVtUq3j4EC>
- N.J. Willis and H.D. Griffiths. 2007. *Advances in Bistatic Radar*. Institution of Engineering and Technology. <https://books.google.de/books?id=HZYOvhgOmzwC>
- Vanessa Wirth, Johanna Bräunig, Danti Khouri, Florian Gutsche, Martin Vossiek, Tim Weyrich, and Marc Stamminger. 2024. Automatic Spatial Calibration of Near-Field MIMO Radar With Respect to Optical Sensors. *ArXiv abs/2403.10981* (2024).
- Di Wu, Matthew O'Toole, Andreas Velten, Amit Agrawal, and Ramesh Raskar. 2012. Decomposing global light transport using time of flight imaging. In *2012 IEEE Conference on Computer Vision and Pattern Recognition*. 366–373. <https://doi.org/10.1109/CVPR.2012.6247697>
- Zhiwei Xiong, Yueyi Zhang, Feng Wu, and Wenjun Zeng. 2017. Computational Depth Sensing : Toward high-performance commodity depth cameras. *IEEE Signal Processing Magazine* 34, 3 (2017), 55–68. <https://doi.org/10.1109/MSP.2017.2669347>
- Pietro Zanuttigh, Ludovico Minto, Giulio Marin, Fabio Dominio, and Guido Cortelazzo. 2016. *Time-of-flight and structured light depth cameras: Technology and applications*. 1–355 pages. <https://doi.org/10.1007/978-3-319-30973-6>
- Natnael S. Zewge, Youngmin Kim, Jintae Kim, and Jong-Hwan Kim. 2019. Millimeter-Wave Radar and RGB-D Camera Sensor Fusion for Real-Time People Detection and Tracking. In *2019 7th International Conference on Robot Intelligence Technology and Applications (RiTA)*. 93–98. <https://doi.org/10.1109/RITAPP.2019.8932892>
- Maxim Zhadobov, Nacer Chahat, Ronan Sauleau, Catherine Le Quement, and Yves Le Dren. 2011. Millimeter-wave interactions with the human body: state of knowledge and recent advances. *International Journal of Microwave and Wireless Technologies* 3, 2 (2011), 237–247. <https://doi.org/10.1017/S1759078711000122>
- Yuri Álvarez López, María García Fernández, Raphael Grau, and Fernando Las-Heras. 2018. A Synthetic Aperture Radar (SAR)-Based Technique for Microwave Imaging and Material Characterization. *Electronics* 7, 12 (2018). <https://doi.org/10.3390/electronics7120373>

11 Spatially Resolved Depth Sensing

It is common practice for stereo sensors to contain two cameras, C_1 and C_2 , of known relative spatial location. In the event of parallel optical axes, this location is defined as the baseline B . To compute depth, pixels in image of C_1 are matched to pixels of C_2 , forming correspondence pairs. For every correspondence pair, the depth d is computed from the disparity D , which represents the difference between their pixel positions [Giancola et al. 2018]:

$$d = f \frac{B}{D}. \quad (13)$$

The depth resolution δ_z of spatially resolved sensors is limited by the disparity resolution ΔD [Zanuttigh et al. 2016]:

$$\delta_z = \frac{z^2}{Bf} \Delta D. \quad (14)$$

We denote the ground truth depth as z and the focal length as f . The disparity resolution is dependent on δ_x and δ_y . For camera-based systems, δ_x and δ_y are typically expressed through the optical transfer function (OTF) [Williams and Becklund 2002].

12 Time Resolved Sensors (Time of Flight)

Time of Flight sensors can be roughly categorized into direct Time of Flight (dToF) and indirect Time of flight (iToF) depth sensing methods. Less common in close range applications are dToF sensors, which send out a signal pulse and directly measure the time it takes for this pulse to be received again. More cost-efficient than dToF are continuous wave (CW) signal modulations that measure time indirectly (iToF) based on the phase shift $\Delta\varphi$ between the transmitted and received signal [Zanuttigh et al. 2016]. The general form of a continuous sinusoidal carrier signal s_c can be described by two equal formulas of traveling time t and traveling distance ρ , respectively:

$$s_c(t) = A \cdot \cos(2\pi t f + \phi_c) \quad (15)$$

$$= A \cdot \underbrace{\cos(2\pi \frac{\rho}{c} f + \phi_c)}_{\varphi} = \widehat{s}_c(\rho) \quad (16)$$

A and f are the known signal amplitude and frequency, respectively and c is the speed of light, φ is the phase and ϕ_c is a constant phase offset. As a transmitted signal $s_t = s_c(t_1) = \widehat{s}_c(\rho_1)$ of known phase and amplitude reflects at a target, the received signal $s_r = s_c(t_2) = \widehat{s}_c(\rho_2)$ has a relative traveling distance of $\Delta\rho = \rho_2 - \rho_1$ between the transmitter and receiver. $\Delta\rho$, is related to the relative phase shift $\Delta\varphi$ [Zanuttigh et al. 2016] by:

$$\Delta\rho = c \frac{\Delta\varphi}{4\pi f} \quad (17)$$

The general assumption of dToF sensors is that a signal directly reflects at the first target and therefore the range (and consequently the depth) is computed as: $r = \frac{\Delta\rho}{2}$.

The depth resolution of a ToF sensor is specific to the utilized wavelength and spatial arrangement of transmitters and receivers. The range resolution of a NIR AMCW ToF sensor can be expressed

as [Lopez Paredes et al. 2023]:

$$\delta_z = \frac{c}{f_m} \sqrt{\frac{P_l + P_a}{P_l} \cdot \frac{I}{k_o q_e \rho \Delta t}} \quad (18)$$

Environment-specific parameters are the power of ambient light P_a , and the reflectivity of the target ρ . Hardware-specific parameters are the modulation frequency f_m , the power of the illumination unit P_l , the total illumination area I , the quantum efficiency q_e , the integration time Δt , and a constant parameter for the optical system, k_o . Due to unknown hardware-specific parameters, we were unable to determine the exact range resolution for NIR AMCW ToF (Azure Kinect) in the sensor parameters table of the main paper. We refer to [Lopez Paredes et al. 2023] for an experimental approach of determining the effective range and lateral resolution.

The spatial resolution of a square-shaped MIMO FSCW imaging sensor can be expressed as [Ahmed 2021]:

$$\delta_{x,y} = \frac{c}{4f_{\max}} \cdot \sqrt{4 \left(\frac{z}{L}\right)^2 + 1} \quad (19)$$

$$\delta_z = \frac{0.5 \cdot c}{\Delta f + \left(1 - \frac{1}{\sqrt{1+0.5(L/z)^2}}\right) \cdot f_{\min}} \quad (20)$$

We denote the size of the square aperture as L .

13 Sensor Settings

The sensor settings in the main paper are chosen with respect to a trade-off between fair sensor comparability and practical applicability. We uniformly list the frame rate computed from the time takes to *capture* the relevant data of one depth frame. Note that this may not necessarily include the computation of depth. For instance, the QAR50 has a capture rate of ≈ 70 fps while the backprojection algorithm has an average computing time of 30 ms such that the overall frame rate is below 1 fps. Furthermore, we manually adjusted each optical sensor's exposure time, if possible, to ensure similar lighting conditions. In summary, we selected the sensor settings that optimize quality while, when feasible, maintaining a comparable frame rate to that of the other sensors. Additionally, we adhered to the manufacturer's recommendations for optimal practical use in interactive applications.

14 Radar Depth Filtering

For our experiments and within the dataset, we chose an empirical threshold of -14 dB over all objects, which — to the best of our knowledge — has proven to yield the best balance of noise pruning while retaining relevant object measurements. In Figure 10, we show how the signal-to-noise ratio of the radar confidence map, i.e., the absolute value of c_{BP} , behaves over different thresholds for the *S1 Hand Open* capture.

15 Radar Material Classification

To investigate the radar signal response and depth deviation with respect to different materials, we divided the 45 objects of MAROON into six classes. These assignments are listed in Table 5. The goal of this classification is to highlight material differences on a coarse level, noting the large object variety that still persists within one

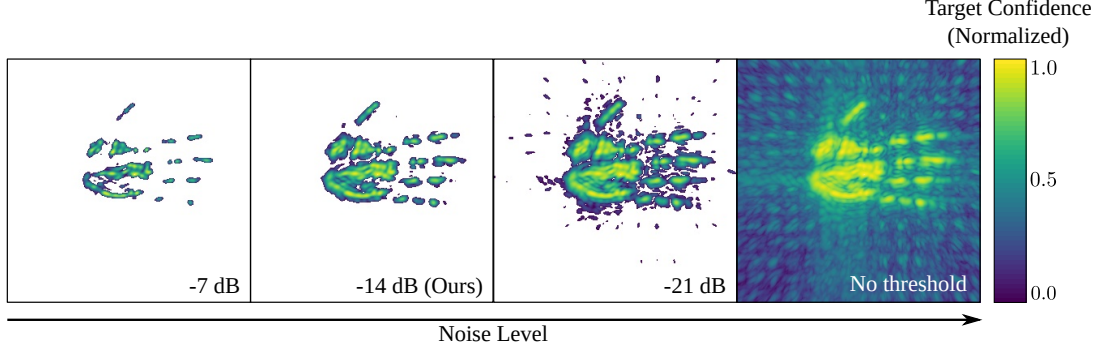


Fig. 10. Visualization of the 2D confidence map from the *S1 Hand Open* capture at various thresholds. The filtered confidence map is subsequently used to extract valid depth information.

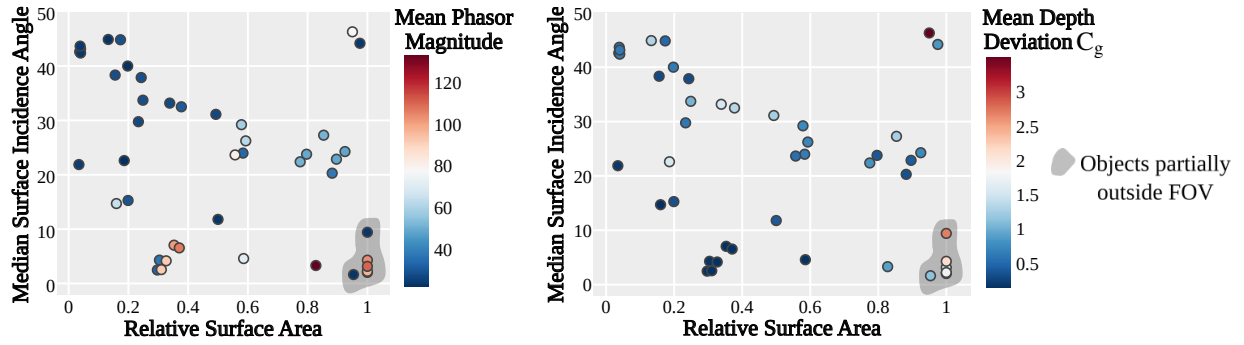


Fig. 11. We present the signal magnitude (*left*) and depth deviation with respect to metric type C_g (*right*) in relation to object geometry (median surface incidence angle) and object size (relative surface area). Large objects outside the radar’s field of view (FOV) exhibit higher depth deviations with respect to the ground truth reconstructions that possibly extend beyond this FOV.

material class. Furthermore, we list the objects that are larger than the antenna aperture, which means they extend partially beyond the radar’s field of view (FOV). It is important to consider these objects when interpreting the depth deviation trends presented in the main paper, as their reconstructions may be incomplete due to the portions that fall outside the FOV, leading to increased depth deviation.

16 Dataset, Additional Results, and Discussion

Example images of all 45 objects in MAROON can be found in Figure 12. For all these objects, we provide additional quantitative results with respect to the depth deviation from the ground truth in Table 6, Table 7, Table 8, and Table 9.

16.1 Discussion of MIMO Radar Signal and Reconstruction

In the main paper, we presented both, the signal magnitude and the depth deviation concerning object material, geometry, and size. To demonstrate that the signal magnitude is not only influenced by either object geometry or by object size — which would be possible due to the high diversity of captured objects that prevents us from isolating one variable while keeping the others constant — we visualize the signal magnitude in Figure 11 (*left*), in relation to object

geometry (median surface incidence angle) and size (relative surface area). A general trend on the x -axis shows an increase in the signal magnitude from left to right, particularly for objects with a surface incidence angle greater than 10° . The majority of objects below this 10° angle on the y -axis exhibit significantly higher signal magnitudes, regardless of their relative surface area, hence indicating the influence of object geometry. On the *right* side of Figure 11, we visualize the mean depth deviation in relation to object geometry and size. While a similar trend is observed for object geometry on the y -axis — where objects of lower surface incidence angle exhibit smaller errors — no overall trend appears on the x -axis, suggesting depth deviation is more influenced by object geometry instead of size.

Class	Objects	Additional Description
Metal	V1 Metal Plate, V2 Metal Plate	
	Metal Disk (Thin), Metal Disk (Thick)	
	Hand Printed: Flat, B, F, U	Coated with metal lacquer
	Brazen Rosette	
	Corner Reflector	
	Cardboard Box	Coated with metal lacquer
	Mirror	Metal surface beneath partially transmissive glass
	Metal Angle	
	Statue	
Fibers and stone	Wood Plane	
	Cardboard	
	Book	Primarily made out of paper
	Concrete Stone	
	Wood Ball	
Polymer	Bunny Box	Large wooden box, comparably small plastic bunny
	Plumber	
	Silicone Cup	
	Christmas Ball: V1, V2, V3	
	Candle	
	Bottle	
	Sandpaper (k120), Sandpaper (k80)	
	Flowerpot (Transparent), Flowerpot (Brown)	
	Polystyrene Plate	
	Water Cube	Water wrapped in a plastic cube
	Scrubber	
	Pool Ball	
	Bunny	
	Tape Dispenser	
Skin	S1 Hand Open, S1 Hand Open (Rev.)	
	S2 Hand Open, S2 Hand Open (Rev.)	
Foam and fabric (Primarily transmissive)	Rubber Foam Plane	
	Sponge	
	Plushie	
	Foam Plane	
Objects outside FOV	Polystyrene Plate	
	Sandpaper (k120), Sandpaper (k80)	
	Wood Plane	
	Foam Plane	
	Rubber Foam Plane	

Table 5. Assignment from objects to material classes with optional description about the assignment process.



Fig. 12. Example images of all objects in MAROON.

	Metric Type	Cardboard	Metal Disk (Thin)	Metal Disk (Thick)	Concrete Stone	Sponge	Wood Ball
RF ToF	C_g	0.13 (\pm 0.06)	<u>0.12</u> (\pm 0.04)	<u>0.12</u> (\pm 0.05)	<u>0.14</u> (\pm 0.07)	<u>1.52</u> (\pm 0.97)	<u>0.59</u> (\pm 0.40)
NIR ToF		0.10 (\pm 0.06)	0.09 (\pm 0.03)	0.08 (\pm 0.05)	0.09 (\pm 0.04)	0.79 (\pm 0.45)	0.17 (\pm 0.12)
Active Stereo		0.08 (\pm 0.05)	0.06 (\pm <u>0.04</u>)	0.07 (\pm 0.05)	0.08 (\pm 0.04)	0.18 (\pm 0.17)	0.13 (\pm 0.06)
Passive Stereo		<u>0.24</u> (\pm 0.11)	0.07 (\pm <u>0.04</u>)	0.08 (\pm 0.07)	0.09 (\pm 0.06)	0.26 (\pm 0.15)	0.34 (\pm 0.16)
RF ToF	C_s	0.15 (\pm 0.08)	<u>0.13</u> (\pm 0.05)	0.13 (\pm 0.06)	<u>0.15</u> (\pm 0.08)	0.54 (\pm 0.40)	0.12 (\pm 0.05)
NIR ToF		0.16 (\pm 0.18)	0.12 (\pm 0.13)	<u>0.14</u> (\pm 0.20)	0.10 (\pm 0.06)	0.79 (\pm 0.42)	0.21 (\pm 0.19)
Active Stereo		0.08 (\pm 0.05)	0.07 (\pm 0.05)	0.08 (\pm 0.07)	0.08 (\pm 0.04)	0.17 (\pm 0.15)	0.13 (\pm 0.07)
Passive Stereo		<u>0.30</u> (\pm 0.13)	0.12 (\pm <u>0.17</u>)	<u>0.14</u> (\pm 0.33)	0.12 (\pm <u>0.08</u>)	0.33 (\pm 0.18)	<u>0.40</u> (\pm <u>0.20</u>)
RF ToF	P	0.13 (\pm 0.14)	0.10 (\pm 0.11)	0.11 (\pm 0.14)	0.13 (\pm 0.15)	<u>2.73</u> (\pm <u>2.47</u>)	0.10 (\pm 0.09)
NIR ToF		0.19 (\pm <u>0.25</u>)	0.13 (\pm 0.19)	0.16 (\pm 0.28)	0.10 (\pm 0.10)	1.32 (\pm 0.58)	0.32 (\pm <u>0.44</u>)
Active Stereo		0.10 (\pm 0.12)	0.08 (\pm 0.25)	0.10 (\pm 0.17)	0.10 (\pm 0.12)	0.29 (\pm 0.42)	0.20 (\pm 0.17)
Passive Stereo		<u>0.36</u> (\pm 0.17)	<u>0.14</u> (\pm <u>0.32</u>)	<u>0.18</u> (\pm 0.51)	<u>0.16</u> (\pm 0.17)	0.47 (\pm 0.51)	<u>0.65</u> (\pm 0.33)
RF ToF	P_e	0.12 (\pm 0.13)	0.10 (\pm 0.08)	<u>0.10</u> (\pm 0.09)	0.13 (\pm 0.15)	2.93 (\pm 2.60)	0.10 (\pm 0.09)
NIR ToF		0.08 (\pm 0.10)	<u>0.12</u> (\pm 0.06)	0.09 (\pm 0.06)	0.09 (\pm 0.07)	1.69 (\pm 0.23)	0.10 (\pm 0.10)
Active Stereo		0.06 (\pm 0.08)	0.06 (\pm 0.06)	0.06 (\pm 0.06)	0.09 (\pm 0.10)	0.42 (\pm 0.50)	0.16 (\pm 0.07)
Passive Stereo		<u>0.38</u> (\pm <u>0.14</u>)	0.08 (\pm <u>0.11</u>)	0.08 (\pm <u>0.10</u>)	0.10 (\pm 0.10)	0.55 (\pm 0.56)	<u>0.69</u> (\pm <u>0.26</u>)
RF ToF	P^*	+0.08 (\pm 0.14)	-0.06 (\pm 0.11)	-0.05 (\pm 0.14)	-0.06 (\pm 0.15)	<u>+2.25</u> (\pm <u>2.47</u>)	-0.07 (\pm 0.09)
NIR ToF		+0.15 (\pm <u>0.25</u>)	-0.04 (\pm 0.19)	-0.01 (\pm 0.28)	-0.08 (\pm 0.10)	+1.30 (\pm 0.58)	+0.09 (\pm <u>0.44</u>)
Active Stereo		+0.04 (\pm 0.12)	-0.01 (\pm 0.25)	-0.02 (\pm 0.17)	-0.04 (\pm 0.12)	-0.15 (\pm 0.42)	+0.17 (\pm 0.17)
Passive Stereo		+0.36 (\pm 0.17)	+0.07 (\pm <u>0.32</u>)	+0.10 (\pm <u>0.51</u>)	+0.15 (\pm 0.17)	+0.22 (\pm 0.51)	+0.64 (\pm 0.33)
RF ToF	P_e^*	+0.08 (\pm 0.13)	-0.09 (\pm 0.08)	<u>-0.08</u> (\pm 0.09)	-0.07 (\pm 0.15)	+2.40 (\pm 2.60)	-0.07 (\pm 0.09)
NIR ToF		-0.00 (\pm 0.10)	<u>-0.12</u> (\pm 0.06)	<u>-0.08</u> (\pm 0.06)	<u>-0.08</u> (\pm 0.07)	+1.69 (\pm 0.23)	-0.05 (\pm 0.10)
Active Stereo		+0.00 (\pm 0.08)	-0.04 (\pm 0.06)	-0.05 (\pm 0.06)	-0.05 (\pm 0.10)	-0.37 (\pm 0.50)	+0.16 (\pm 0.07)
Passive Stereo		+0.38 (\pm <u>0.14</u>)	+0.01 (\pm <u>0.11</u>)	+0.02 (\pm <u>0.10</u>)	+0.08 (\pm 0.10)	-0.34 (\pm 0.56)	+0.69 (\pm <u>0.26</u>)

	Metric Type	Scrubber	Cardboard Box	Plushie	Bottle	Tape Dispenser	Book
RF ToF	C_g	0.58 (\pm 0.29)	0.12 (\pm 0.08)	<u>0.81</u> (\pm 0.47)	<u>1.22</u> (\pm 1.00)	0.31 (\pm 0.23)	0.37 (\pm 0.56)
NIR ToF		<u>0.64</u> (\pm 0.34)	0.11 (\pm 0.04)	0.49 (\pm 0.21)	0.44 (\pm 0.51)	<u>0.84</u> (\pm 0.30)	<u>0.59</u> (\pm 0.65)
Active Stereo		0.20 (\pm 0.16)	0.12 (\pm 0.07)	0.13 (\pm 0.14)	0.16 (\pm 0.21)	0.16 (\pm 0.14)	0.13 (\pm 0.11)
Passive Stereo		0.14 (\pm 0.11)	<u>0.29</u> (\pm <u>0.20</u>)	0.19 (\pm 0.21)	0.28 (\pm 0.36)	0.15 (\pm 0.11)	0.15 (\pm 0.13)
RF ToF	C_s	<u>0.97</u> (\pm 0.61)	0.11 (\pm 0.05)	2.21 (\pm 2.05)	0.49 (\pm 0.99)	0.55 (\pm 0.77)	0.14 (\pm 0.08)
NIR ToF		0.59 (\pm 0.30)	0.14 (\pm 0.16)	0.53 (\pm 0.28)	<u>0.80</u> (\pm 1.32)	<u>1.16</u> (\pm 0.60)	0.20 (\pm 0.17)
Active Stereo		0.17 (\pm 0.11)	0.15 (\pm 0.13)	0.12 (\pm 0.38)	0.20 (\pm 0.53)	0.17 (\pm 0.17)	0.18 (\pm 0.15)
Passive Stereo		0.19 (\pm 0.13)	<u>0.35</u> (\pm <u>0.24</u>)	0.23 (\pm 0.27)	0.41 (\pm 0.62)	0.22 (\pm 0.20)	<u>0.24</u> (\pm 0.19)
RF ToF	P	<u>1.28</u> (\pm 0.76)	0.38 (\pm <u>1.52</u>)	<u>3.64</u> (\pm 3.23)	0.64 (\pm 1.63)	0.67 (\pm 1.08)	0.13 (\pm 0.31)
NIR ToF		0.91 (\pm 0.47)	0.14 (\pm 0.19)	<u>0.85</u> (\pm 0.52)	<u>1.32</u> (\pm 2.00)	<u>1.57</u> (\pm 0.70)	<u>1.15</u> (\pm 1.42)
Active Stereo		0.27 (\pm 0.34)	0.19 (\pm 0.22)	0.24 (\pm 1.25)	0.49 (\pm 2.49)	0.24 (\pm 0.35)	0.19 (\pm 0.25)
Passive Stereo		0.29 (\pm 0.38)	<u>0.47</u> (\pm 0.55)	0.35 (\pm 0.54)	0.62 (\pm 0.97)	0.29 (\pm 0.35)	0.47 (\pm 1.21)
RF ToF	P_e	<u>1.35</u> (\pm 0.66)	0.25 (\pm <u>1.19</u>)	<u>3.61</u> (\pm 3.23)	0.63 (\pm 1.63)	0.66 (\pm 1.07)	0.13 (\pm 0.30)
NIR ToF		1.16 (\pm 0.27)	0.13 (\pm 0.07)	0.82 (\pm 0.38)	<u>1.16</u> (\pm 2.16)	<u>1.70</u> (\pm 0.89)	<u>1.34</u> (\pm 1.54)
Active Stereo		0.22 (\pm 0.27)	0.18 (\pm 0.12)	0.16 (\pm 0.30)	0.33 (\pm 1.13)	0.15 (\pm 0.21)	0.17 (\pm 0.23)
Passive Stereo		0.24 (\pm 0.29)	<u>0.42</u> (\pm 0.28)	0.18 (\pm 0.26)	0.55 (\pm 0.86)	0.20 (\pm 0.22)	0.33 (\pm 0.95)
RF ToF	P^*	+1.26 (\pm 0.76)	+0.28 (\pm 1.52)	+3.63 (\pm 3.23)	+0.52 (\pm 1.63)	+0.56 (\pm 1.08)	-0.10 (\pm 0.31)
NIR ToF		+0.89 (\pm 0.47)	-0.09 (\pm 0.19)	+0.80 (\pm 0.52)	+1.30 (\pm 2.00)	+1.57 (\pm 0.70)	+1.13 (\pm 1.42)
Active Stereo		-0.01 (\pm 0.34)	-0.10 (\pm 0.22)	-0.04 (\pm 1.25)	+0.18 (\pm 2.49)	+0.01 (\pm 0.35)	-0.07 (\pm 0.25)
Passive Stereo		-0.01 (\pm 0.38)	+0.42 (\pm 0.55)	+0.17 (\pm 0.54)	+0.51 (\pm 0.97)	+0.19 (\pm 0.35)	+0.39 (\pm 1.21)
RF ToF	P_e^*	+1.34 (\pm 0.66)	+0.14 (\pm <u>1.19</u>)	+3.59 (\pm 3.23)	+0.52 (\pm 1.63)	+0.57 (\pm 1.07)	-0.10 (\pm 0.30)
NIR ToF		+1.16 (\pm 0.27)	-0.13 (\pm 0.07)	+0.82 (\pm 0.38)	+1.15 (\pm 2.16)	+1.70 (\pm 0.89)	+1.33 (\pm 1.54)
Active Stereo		-0.02 (\pm 0.27)	-0.16 (\pm 0.12)	-0.06 (\pm 0.30)	+0.21 (\pm 1.13)	+0.03 (\pm 0.21)	-0.02 (\pm 0.23)
Passive Stereo		-0.07 (\pm 0.29)	+0.42 (\pm 0.28)	+0.02 (\pm 0.26)	+0.52 (\pm 0.86)	+0.08 (\pm 0.22)	+0.27 (\pm 0.95)

Table 6. We measure the sensor-GT deviation with respect to C_g , C_s , P , P_e and an additional signed version of P, P_e , which is denoted as P^*, P_e^* . All metrics are listed in the form $(\mu \pm \sigma)$, consisting of the mean μ and standard deviation σ in centimeters, computed over the entire metric domain, respectively. The best results among all sensors of one metric type are highlighted in **bold** and the worst results are underlined.

	Metric Type	Statue	Rubber Foam Plane	Sandpaper (k80)	Sandpaper (k120)	Wood Plane	Foam Plane
RF ToF	C_g	0.27 (\pm 0.25)	<u>1.10</u> (\pm 1.21)	<u>1.70</u> (\pm 2.07)	<u>1.71</u> (\pm 2.23)	<u>2.08</u> (\pm 2.31)	<u>2.66</u> (\pm 1.26)
NIR ToF		0.32 (\pm 0.28)	0.34 (\pm 0.07)	0.09 (\pm 0.04)	0.07 (\pm 0.03)	0.48 (\pm 0.15)	0.80 (\pm 0.14)
Active Stereo		0.16 (\pm 0.13)	0.11 (\pm 0.05)	0.07 (\pm 0.04)	0.08 (\pm 0.04)	0.13 (\pm 0.06)	0.08 (\pm 0.06)
Passive Stereo		0.13 (\pm 0.13)	0.77 (\pm 0.67)	0.08 (\pm 0.04)	0.10 (\pm 0.06)	0.12 (\pm 0.10)	0.15 (\pm 0.09)
RF ToF	C_s	0.17 (\pm 0.11)	0.34 (\pm <u>0.72</u>)	<u>0.12</u> (\pm 0.05)	<u>0.12</u> (\pm 0.05)	0.20 (\pm 0.12)	<u>2.83</u> (\pm <u>0.89</u>)
NIR ToF		<u>0.43</u> (\pm 0.42)	0.38 (\pm 0.11)	0.11 (\pm <u>0.12</u>)	0.09 (\pm <u>0.12</u>)	<u>0.52</u> (\pm <u>0.16</u>)	0.84 (\pm 0.15)
Active Stereo		0.19 (\pm <u>0.76</u>)	0.13 (\pm 0.08)	0.08 (\pm 0.05)	0.09 (\pm 0.05)	0.15 (\pm 0.08)	0.09 (\pm 0.15)
Passive Stereo		0.18 (\pm 0.69)	<u>0.83</u> (\pm 0.71)	<u>0.12</u> (\pm 0.09)	0.11 (\pm 0.08)	0.13 (\pm 0.11)	0.16 (\pm 0.12)
RF ToF	P	0.20 (\pm 0.26)	<u>1.62</u> (\pm 2.21)	0.09 (\pm 0.11)	0.08 (\pm 0.10)	0.18 (\pm 0.23)	3.95 (\pm 4.22)
NIR ToF		0.77 (\pm 3.13)	0.44 (\pm 0.19)	0.10 (\pm 0.14)	0.09 (\pm <u>0.14</u>)	<u>0.65</u> (\pm <u>0.28</u>)	1.13 (\pm 3.58)
Active Stereo		0.90 (\pm 5.17)	0.16 (\pm 0.24)	0.09 (\pm 0.09)	0.10 (\pm 0.09)	0.20 (\pm 0.12)	0.21 (\pm 2.11)
Passive Stereo		<u>1.43</u> (\pm <u>7.09</u>)	0.91 (\pm 1.11)	<u>0.13</u> (\pm 0.17)	<u>0.13</u> (\pm 0.14)	0.14 (\pm 0.18)	0.19 (\pm 0.44)
RF ToF	P_e	0.20 (\pm <u>0.27</u>)	<u>1.62</u> (\pm <u>2.21</u>)	0.09 (\pm 0.11)	0.08 (\pm 0.10)	0.18 (\pm 0.23)	<u>3.95</u> (\pm <u>4.22</u>)
NIR ToF		<u>0.25</u> (\pm 0.13)	0.43 (\pm 0.11)	0.08 (\pm 0.10)	0.08 (\pm 0.10)	<u>0.64</u> (\pm <u>0.27</u>)	0.91 (\pm 0.12)
Active Stereo		0.16 (\pm 0.21)	0.16 (\pm 0.09)	0.09 (\pm 0.08)	0.10 (\pm 0.09)	0.20 (\pm 0.10)	0.09 (\pm 0.10)
Passive Stereo		0.10 (\pm 0.13)	0.94 (\pm 1.13)	<u>0.12</u> (\pm 0.15)	<u>0.11</u> (\pm 0.12)	0.12 (\pm 0.13)	0.17 (\pm 0.20)
RF ToF	P^*	-0.04 (\pm 0.26)	<u>-1.35</u> (\pm <u>2.21</u>)	-0.04 (\pm 0.11)	-0.04 (\pm 0.10)	+0.03 (\pm 0.23)	-0.66 (\pm 4.22)
NIR ToF		-0.23 (\pm 3.13)	+0.43 (\pm 0.19)	-0.03 (\pm 0.14)	+0.02 (\pm <u>0.14</u>)	<u>+0.65</u> (\pm <u>0.28</u>)	<u>+1.13</u> (\pm 3.58)
Active Stereo		+0.71 (\pm 5.17)	-0.15 (\pm 0.24)	<u>-0.06</u> (\pm 0.09)	<u>-0.08</u> (\pm 0.09)	-0.19 (\pm 0.12)	+0.08 (\pm 2.11)
Passive Stereo		<u>+1.34</u> (\pm <u>7.09</u>)	+0.34 (\pm 1.11)	+0.00 (\pm <u>0.17</u>)	<u>-0.08</u> (\pm <u>0.14</u>)	+0.08 (\pm 0.18)	+0.08 (\pm 0.44)
RF ToF	P_e^*	-0.04 (\pm <u>0.27</u>)	<u>-1.35</u> (\pm <u>2.21</u>)	-0.04 (\pm 0.11)	-0.04 (\pm 0.10)	+0.03 (\pm 0.23)	-0.66 (\pm 4.22)
NIR ToF		<u>-0.24</u> (\pm 0.13)	+0.43 (\pm 0.11)	-0.04 (\pm 0.10)	+0.00 (\pm 0.10)	<u>+0.64</u> (\pm <u>0.27</u>)	<u>+0.91</u> (\pm 0.12)
Active Stereo		+0.07 (\pm 0.21)	-0.16 (\pm 0.09)	<u>-0.06</u> (\pm 0.08)	<u>-0.09</u> (\pm 0.09)	-0.20 (\pm 0.10)	-0.05 (\pm 0.10)
Passive Stereo		+0.03 (\pm 0.13)	+0.35 (\pm 1.13)	+0.01 (\pm <u>0.15</u>)	-0.07 (\pm <u>0.12</u>)	+0.07 (\pm 0.13)	+0.07 (\pm 0.20)

	Metric Type	S1 Hand Open	S1 Hand Open (Rev.)	S2 Hand Open	S2 Hand Open (Rev.)	Hand Printed Flat	Corner Reflector
RF ToF	C_g	0.36 (\pm 0.38)	<u>1.23</u> (\pm 1.42)	0.39 (\pm 0.37)	0.79 (\pm 0.79)	0.71 (\pm 0.78)	3.48 (\pm 1.80)
NIR ToF		0.31 (\pm 0.14)	0.27 (\pm 0.12)	0.19 (\pm 0.10)	0.21 (\pm 0.11)	0.25 (\pm 0.12)	1.81 (\pm 1.01)
Active Stereo		0.12 (\pm 0.09)	0.16 (\pm 0.15)	0.16 (\pm 0.13)	0.21 (\pm 0.16)	0.09 (\pm 0.07)	0.48 (\pm 0.62)
Passive Stereo		0.20 (\pm 0.16)	0.12 (\pm 0.09)	0.20 (\pm 0.16)	0.20 (\pm 0.15)	0.21 (\pm 0.37)	0.30 (\pm 0.29)
RF ToF	C_s	0.22 (\pm 0.15)	0.17 (\pm 0.11)	0.20 (\pm 0.14)	0.15 (\pm 0.09)	0.17 (\pm 0.13)	1.95 (\pm 0.94)
NIR ToF		<u>0.38</u> (\pm <u>0.26</u>)	<u>0.32</u> (\pm 0.24)	<u>0.25</u> (\pm <u>0.23</u>)	<u>0.27</u> (\pm 0.24)	<u>0.29</u> (\pm 0.20)	<u>1.97</u> (\pm 1.09)
Active Stereo		0.13 (\pm 0.10)	0.18 (\pm <u>0.73</u>)	0.17 (\pm 0.14)	0.22 (\pm 0.15)	0.09 (\pm 0.06)	0.55 (\pm <u>1.54</u>)
Passive Stereo		0.26 (\pm 0.22)	0.17 (\pm 0.18)	<u>0.25</u> (\pm 0.20)	0.25 (\pm 0.19)	0.18 (\pm <u>0.34</u>)	0.61 (\pm 1.22)
RF ToF	P	0.22 (\pm 0.25)	0.16 (\pm 0.21)	0.20 (\pm 0.24)	0.14 (\pm 0.17)	0.16 (\pm 0.20)	<u>3.31</u> (\pm 1.53)
NIR ToF		<u>0.52</u> (\pm 0.43)	<u>0.47</u> (\pm 0.44)	<u>0.39</u> (\pm 0.57)	<u>0.35</u> (\pm 0.39)	0.33 (\pm 0.29)	2.87 (\pm 1.67)
Active Stereo		0.22 (\pm <u>1.25</u>)	0.30 (\pm <u>1.54</u>)	0.29 (\pm <u>1.67</u>)	0.33 (\pm <u>1.09</u>)	0.16 (\pm 1.30)	1.06 (\pm <u>3.92</u>)
Passive Stereo		0.35 (\pm 0.41)	0.22 (\pm 0.38)	0.35 (\pm 0.85)	0.32 (\pm 0.48)	<u>1.73</u> (\pm <u>8.95</u>)	0.99 (\pm 2.49)
RF ToF	P_e	0.22 (\pm 0.25)	0.16 (\pm 0.20)	0.20 (\pm 0.24)	0.14 (\pm 0.16)	0.16 (\pm 0.20)	3.14 (\pm 1.41)
NIR ToF		<u>0.51</u> (\pm 0.27)	<u>0.38</u> (\pm 0.21)	<u>0.30</u> (\pm 0.22)	0.25 (\pm 0.17)	<u>0.30</u> (\pm 0.09)	2.65 (\pm 1.29)
Active Stereo		0.16 (\pm 0.24)	0.20 (\pm <u>0.25</u>)	0.20 (\pm 0.23)	<u>0.26</u> (\pm <u>0.30</u>)	0.08 (\pm 0.10)	0.70 (\pm 0.92)
Passive Stereo		0.25 (\pm <u>0.34</u>)	0.16 (\pm 0.17)	0.21 (\pm <u>0.25</u>)	0.25 (\pm 0.21)	0.17 (\pm 0.15)	1.26 (\pm <u>1.63</u>)
RF ToF	P^*	-0.15 (\pm 0.25)	-0.06 (\pm 0.21)	-0.10 (\pm 0.24)	-0.07 (\pm 0.17)	-0.07 (\pm 0.20)	<u>+3.31</u> (\pm 1.53)
NIR ToF		<u>+0.49</u> (\pm 0.43)	<u>+0.42</u> (\pm 0.44)	<u>+0.32</u> (\pm 0.57)	<u>+0.29</u> (\pm 0.39)	-0.30 (\pm 0.29)	+2.86 (\pm 1.67)
Active Stereo		+0.06 (\pm <u>1.25</u>)	-0.07 (\pm <u>1.54</u>)	-0.04 (\pm <u>1.67</u>)	+0.12 (\pm <u>1.09</u>)	+0.04 (\pm 1.30)	+0.82 (\pm <u>3.92</u>)
Passive Stereo		+0.22 (\pm 0.41)	+0.17 (\pm 0.38)	+0.32 (\pm 0.85)	<u>+0.29</u> (\pm 0.48)	<u>+1.70</u> (\pm <u>8.95</u>)	+0.88 (\pm 2.49)
RF ToF	P_e^*	-0.14 (\pm 0.25)	-0.06 (\pm 0.20)	-0.10 (\pm 0.24)	-0.07 (\pm 0.16)	-0.07 (\pm 0.20)	<u>+3.14</u> (\pm 1.41)
NIR ToF		<u>+0.51</u> (\pm 0.27)	<u>+0.38</u> (\pm 0.21)	<u>+0.28</u> (\pm 0.22)	<u>+0.24</u> (\pm 0.17)	<u>-0.30</u> (\pm 0.09)	+2.65 (\pm 1.29)
Active Stereo		+0.00 (\pm 0.24)	-0.13 (\pm <u>0.25</u>)	-0.14 (\pm 0.23)	+0.11 (\pm <u>0.30</u>)	+0.00 (\pm 0.10)	+0.45 (\pm 0.92)
Passive Stereo		+0.05 (\pm <u>0.34</u>)	+0.11 (\pm 0.17)	+0.15 (\pm <u>0.25</u>)	+0.23 (\pm 0.21)	+0.16 (\pm 0.15)	+1.23 (\pm <u>1.63</u>)

Table 7. We measure the sensor-GT deviation with respect to C_g , C_s , P, P_e and an additional signed version of P, P_e , which is denoted as P^* , P_e^* . All metrics are listed in the form ($\mu \pm \sigma$), consisting of the mean μ and standard deviation σ in centimeters, computed over the entire metric domain, respectively. The best results among all sensors of one metric type are highlighted in **bold** and the worst results are underlined.

	Metric Type	Mirror	Candle	Flowerpot (Transparent)	V1 Metal Plate	V2 Metal Plate	Hand Printed F
RF ToF	C_g	0.87 (± 0.26)	1.50 (± 1.12)	1.31 (± 1.21)	0.12 (± 0.05)	0.12 (± 0.05)	<u>0.69</u> (± 0.86)
NIR ToF		3.77 (± 1.97)	2.04 (± 0.40)	<u>2.73</u> (± 1.03)	0.77 (± 0.42)	<u>0.74</u> (± 0.45)	0.12 (± 0.09)
Active Stereo		2.13 (± 1.52)	0.26 (± 0.29)	0.74 (± 0.53)	0.08 (± 0.06)	0.30 (± 0.29)	0.17 (± 0.18)
Passive Stereo		2.31 (± 1.61)	1.64 (± 0.78)	2.01 (± 0.83)	0.13 (± 0.07)	0.15 (± 0.11)	0.20 (± 0.14)
RF ToF	C_s	0.91 (± 0.14)	<u>5.57</u> (± 2.78)	1.86 (± 2.41)	0.13 (± 0.06)	0.13 (± 0.07)	0.15 (± 0.10)
NIR ToF		<u>33.31</u> (± 9.07)	1.71 (± 0.49)	<u>3.10</u> (± 1.22)	<u>0.81</u> (± 0.43)	<u>15.66</u> (± 17.32)	0.12 (± 0.10)
Active Stereo		30.21 (± 14.59)	0.25 (± 0.26)	1.27 (± 1.78)	0.09 (± 0.07)	5.54 (± 12.95)	0.21 (± 0.63)
Passive Stereo		27.02 (± 11.33)	1.28 (± 0.65)	1.86 (± 0.93)	0.16 (± 0.11)	0.20 (± 0.14)	<u>0.23</u> (± 0.16)
RF ToF	P	0.93 (± 0.12)	<u>7.41</u> (± 3.79)	2.74 (± 3.66)	0.11 (± 0.12)	0.11 (± 0.12)	0.14 (± 0.20)
NIR ToF		37.84 (± 14.84)	2.78 (± 0.35)	<u>5.24</u> (± 2.04)	<u>0.95</u> (± 0.48)	<u>16.23</u> (± 18.21)	0.17 (± 0.30)
Active Stereo		<u>39.66</u> (± 24.75)	0.42 (± 0.49)	2.08 (± 2.30)	0.10 (± 0.13)	6.16 (± 13.78)	<u>0.56</u> (± 2.02)
Passive Stereo		30.82 (± 14.01)	2.10 (± 0.98)	3.50 (± 1.37)	0.19 (± 0.15)	0.22 (± 0.20)	0.43 (± 0.73)
RF ToF	P_e	0.93 (± 0.12)	<u>7.37</u> (± 3.85)	2.76 (± 3.66)	0.10 (± 0.11)	0.11 (± 0.12)	0.13 (± 0.20)
NIR ToF		39.68 (± 6.57)	2.75 (± 0.15)	<u>6.18</u> (± 1.79)	<u>0.79</u> (± 0.39)	<u>24.92</u> (± 17.59)	0.13 (± 0.16)
Active Stereo		43.84 (± 20.28)	0.31 (± 0.44)	2.52 (± 1.77)	0.07 (± 0.09)	7.46 (± 14.94)	0.53 (± 1.07)
Passive Stereo		35.96 (± 7.83)	2.15 (± 0.65)	4.36 (± 0.71)	0.15 (± 0.09)	0.23 (± 0.19)	0.34 (± 0.65)
RF ToF	P^*	+0.93 (± 0.12)	<u>+7.38</u> (± 3.79)	+2.68 (± 3.66)	-0.06 (± 0.12)	-0.06 (± 0.12)	-0.02 (± 0.20)
NIR ToF		+37.84 (± 14.84)	+2.78 (± 0.35)	<u>+5.24</u> (± 2.04)	<u>+0.95</u> (± 0.48)	<u>+16.21</u> (± 18.21)	<u>-0.11</u> (± 0.30)
Active Stereo		<u>+39.58</u> (± 24.75)	+0.37 (± 0.49)	+2.00 (± 2.30)	+0.00 (± 0.13)	+5.77 (± 13.78)	-0.03 (± 2.02)
Passive Stereo		+30.80 (± 14.01)	+2.10 (± 0.98)	+3.49 (± 1.37)	+0.17 (± 0.15)	+0.19 (± 0.20)	+0.02 (± 0.73)
RF ToF	P_e^*	+0.93 (± 0.12)	<u>+7.34</u> (± 3.85)	+2.70 (± 3.66)	-0.06 (± 0.11)	-0.06 (± 0.12)	-0.01 (± 0.20)
NIR ToF		+39.68 (± 6.57)	+2.75 (± 0.15)	+6.18 (± 1.79)	+0.79 (± 0.39)	<u>+24.90</u> (± 17.59)	-0.11 (± 0.16)
Active Stereo		<u>+43.84</u> (± 20.28)	+0.27 (± 0.44)	+2.52 (± 1.77)	+0.01 (± 0.09)	+7.08 (± 14.94)	<u>-0.36</u> (± 1.07)
Passive Stereo		+35.96 (± 7.83)	+2.15 (± 0.65)	+4.36 (± 0.71)	+0.15 (± 0.09)	+0.21 (± 0.19)	-0.07 (± 0.65)

	Metric Type	Hand Printed B	Hand Printed U	Metal Angle	Plunger	Silicone Cup	V1 Christmas Ball
RF ToF	C_g	<u>0.52</u> (± 0.70)	<u>0.72</u> (± 0.80)	0.47 (± 0.28)	0.62 (± 0.60)	<u>0.60</u> (± 0.47)	<u>0.59</u> (± 0.40)
NIR ToF		0.09 (± 0.06)	0.12 (± 0.09)	<u>0.90</u> (± 0.79)	0.23 (± 0.13)	0.16 (± 0.10)	0.22 (± 0.14)
Active Stereo		0.12 (± 0.11)	0.15 (± 0.12)	0.23 (± 0.18)	0.24 (± 0.17)	0.13 (± 0.10)	0.13 (± 0.09)
Passive Stereo		0.19 (± 0.16)	0.18 (± 0.14)	<u>0.24</u> (± 0.17)	<u>0.95</u> (± 0.64)	0.15 (± 0.10)	0.13 (± 0.05)
RF ToF	C_s	0.17 (± 0.12)	0.18 (± 0.13)	<u>1.20</u> (± 0.87)	<u>1.18</u> (± 2.39)	<u>1.43</u> (± 1.49)	<u>0.75</u> (± 0.95)
NIR ToF		0.10 (± 0.12)	0.14 (± 0.15)	1.02 (± 0.54)	0.28 (± 0.19)	0.21 (± 0.22)	0.41 (± 0.34)
Active Stereo		0.13 (± 0.25)	0.17 (± 0.51)	0.29 (± 0.32)	0.29 (± 0.32)	0.13 (± 0.10)	0.14 (± 0.09)
Passive Stereo		<u>0.20</u> (± 0.21)	<u>0.22</u> (± 0.22)	0.49 (± 0.57)	0.87 (± 0.63)	0.17 (± 0.14)	0.24 (± 0.15)
RF ToF	P	0.17 (± 0.23)	0.19 (± 0.28)	<u>1.71</u> (± 1.47)	<u>1.47</u> (± 2.94)	<u>2.33</u> (± 2.79)	<u>1.05</u> (± 1.41)
NIR ToF		0.17 (± 0.33)	0.23 (± 0.45)	1.68 (± 1.29)	0.42 (± 0.54)	0.30 (± 0.38)	0.62 (± 0.64)
Active Stereo		0.26 (± 1.15)	<u>0.46</u> (± 2.16)	0.49 (± 0.69)	0.55 (± 0.96)	0.20 (± 0.28)	0.22 (± 0.25)
Passive Stereo		<u>0.33</u> (± 0.54)	0.37 (± 0.62)	0.76 (± 0.88)	1.33 (± 1.35)	0.27 (± 0.37)	0.35 (± 0.22)
RF ToF	P_e	0.17 (± 0.23)	0.19 (± 0.28)	<u>1.79</u> (± 1.47)	1.62 (± 3.10)	2.55 (± 2.95)	<u>1.05</u> (± 1.41)
NIR ToF		0.08 (± 0.11)	0.16 (± 0.22)	1.40 (± 0.76)	0.27 (± 0.25)	0.23 (± 0.27)	0.36 (± 0.37)
Active Stereo		0.18 (± 0.25)	0.28 (± 0.45)	0.52 (± 0.74)	0.58 (± 0.78)	0.16 (± 0.16)	0.15 (± 0.19)
Passive Stereo		<u>0.28</u> (± 0.40)	<u>0.40</u> (± 0.58)	0.67 (± 0.50)	<u>1.71</u> (± 0.66)	0.25 (± 0.21)	0.44 (± 0.23)
RF ToF	P^*	-0.02 (± 0.23)	+0.00 (± 0.28)	+1.56 (± 1.47)	<u>+0.89</u> (± 2.94)	<u>+2.08</u> (± 2.79)	<u>+0.96</u> (± 1.41)
NIR ToF		+0.02 (± 0.33)	-0.01 (± 0.45)	<u>+1.66</u> (± 1.29)	+0.31 (± 0.54)	+0.22 (± 0.38)	+0.50 (± 0.64)
Active Stereo		-0.03 (± 1.15)	<u>+0.15</u> (± 2.16)	+0.40 (± 0.69)	-0.32 (± 0.96)	+0.05 (± 0.28)	+0.18 (± 0.25)
Passive Stereo		<u>+0.08</u> (± 0.54)	<u>+0.15</u> (± 0.62)	+0.72 (± 0.88)	<u>-0.89</u> (± 1.35)	+0.17 (± 0.37)	+0.34 (± 0.22)
RF ToF	P_e^*	-0.01 (± 0.23)	+0.00 (± 0.28)	+1.63 (± 1.47)	+0.96 (± 3.10)	+2.27 (± 2.95)	<u>+0.96</u> (± 1.41)
NIR ToF		-0.02 (± 0.11)	-0.04 (± 0.22)	+1.37 (± 0.76)	+0.26 (± 0.25)	+0.19 (± 0.27)	+0.30 (± 0.37)
Active Stereo		<u>-0.08</u> (± 0.25)	-0.02 (± 0.45)	+0.39 (± 0.74)	-0.55 (± 0.78)	+0.12 (± 0.16)	+0.14 (± 0.19)
Passive Stereo		-0.00 (± 0.40)	<u>+0.05</u> (± 0.58)	+0.65 (± 0.50)	<u>-1.71</u> (± 0.66)	+0.22 (± 0.21)	+0.44 (± 0.23)

Table 8. We measure the sensor-GT deviation with respect to C_g , C_s , P , P_e and an additional signed version of P, P_e , which is denoted as P^*, P_e^* . All metrics are listed in the form $(\mu \pm \sigma)$, consisting of the mean μ and standard deviation σ in centimeters, computed over the entire metric domain, respectively. The best results among all sensors of one metric type are highlighted in **bold** and the worst results are underlined.

	Metric Type	V2 Christmas Ball	V3 Christmas Ball	Water Cube	Flowerpot (Brown)	Brazen Rosette	Pool Ball
RF ToF	C_g	<u>0.59</u> (± 0.40)	<u>0.60</u> (± 0.41)	0.16 (± 0.11)	<u>1.00</u> (± 0.90)	0.11 (± 0.08)	<u>1.28</u> (± 0.78)
NIR ToF		0.28 (± 0.18)	0.47 (± 0.24)	<u>3.00</u> (± 0.44)	0.15 (± 0.08)	<u>0.94</u> (± 0.35)	0.64 (± 0.17)
Active Stereo		0.51 (± 0.22)	0.50 (± 0.20)	0.56 (± 0.17)	0.12 (± 0.21)	0.36 (± 0.24)	0.31 (± 0.25)
Passive Stereo		0.46 (± 0.17)	0.30 (± 0.13)	0.46 (± 0.24)	0.45 (± 0.25)	0.18 (± 0.13)	0.87 (± 0.30)
RF ToF	C_s	0.10 (± 0.03)	0.10 (± 0.03)	0.12 (± 0.06)	<u>0.53</u> (± 1.23)	0.11 (± 0.05)	0.09 (± 0.03)
NIR ToF		<u>0.80</u> (± 0.80)	<u>1.66</u> (± 1.65)	<u>2.88</u> (± 0.54)	0.22 (± 0.27)	<u>8.11</u> (± 11.87)	0.69 (± 0.35)
Active Stereo		0.43 (± 0.23)	0.39 (± 0.22)	0.54 (± 0.27)	0.10 (± 0.09)	0.46 (± 0.45)	0.33 (± 0.27)
Passive Stereo		0.46 (± 0.21)	0.39 (± 0.21)	0.52 (± 0.28)	0.49 (± 0.27)	0.29 (± 0.29)	<u>0.71</u> (± 0.35)
RF ToF	P	0.07 (± 0.06)	0.08 (± 0.08)	0.10 (± 0.10)	<u>0.77</u> (± 1.96)	0.09 (± 0.13)	0.05 (± 0.07)
NIR ToF		<u>1.05</u> (± 1.29)	<u>3.19</u> (± 6.90)	<u>3.99</u> (± 0.84)	0.37 (± 0.46)	<u>9.03</u> (± 12.38)	1.06 (± 0.48)
Active Stereo		0.66 (± 0.24)	0.64 (± 0.25)	0.89 (± 0.35)	0.16 (± 0.26)	0.72 (± 0.82)	0.50 (± 0.38)
Passive Stereo		0.72 (± 0.22)	0.59 (± 0.23)	0.84 (± 0.35)	0.67 (± 0.37)	0.39 (± 0.48)	<u>1.15</u> (± 0.30)
RF ToF	P_e	0.07 (± 0.06)	0.08 (± 0.08)	0.10 (± 0.10)	<u>0.78</u> (± 1.97)	0.09 (± 0.13)	0.05 (± 0.07)
NIR ToF		0.36 (± 0.57)	<u>1.77</u> (± 2.11)	<u>4.97</u> (± 0.27)	0.15 (± 0.11)	<u>15.00</u> (± 13.89)	0.96 (± 0.18)
Active Stereo		0.75 (± 0.21)	0.73 (± 0.15)	0.86 (± 0.19)	0.10 (± 0.12)	0.76 (± 0.78)	0.52 (± 0.37)
Passive Stereo		<u>0.85</u> (± 0.16)	0.70 (± 0.18)	1.17 (± 0.05)	<u>0.81</u> (± 0.25)	0.40 (± 0.44)	<u>1.29</u> (± 0.18)
RF ToF	P^*	-0.05 (± 0.06)	-0.05 (± 0.08)	+0.08 (± 0.10)	<u>+0.67</u> (± 1.96)	-0.02 (± 0.13)	+0.01 (± 0.07)
NIR ToF		<u>+0.68</u> (± 1.29)	<u>+3.08</u> (± 6.90)	<u>+3.99</u> (± 0.84)	<u>+0.36</u> (± 0.46)	<u>+9.01</u> (± 12.38)	<u>+1.05</u> (± 0.48)
Active Stereo		<u>+0.66</u> (± 0.24)	<u>+0.63</u> (± 0.25)	<u>+0.88</u> (± 0.35)	-0.07 (± 0.26)	<u>-0.62</u> (± 0.82)	<u>+0.48</u> (± 0.38)
Passive Stereo		<u>+0.72</u> (± 0.22)	<u>+0.59</u> (± 0.23)	<u>+0.83</u> (± 0.35)	<u>+0.66</u> (± 0.37)	<u>-0.23</u> (± 0.48)	<u>+1.15</u> (± 0.30)
RF ToF	P_e^*	-0.05 (± 0.06)	-0.05 (± 0.08)	+0.08 (± 0.10)	<u>+0.68</u> (± 1.97)	-0.02 (± 0.13)	+0.01 (± 0.07)
NIR ToF		<u>+0.17</u> (± 0.57)	<u>+1.72</u> (± 2.11)	<u>+4.97</u> (± 0.27)	<u>+0.15</u> (± 0.11)	<u>+14.97</u> (± 13.89)	<u>+0.96</u> (± 0.18)
Active Stereo		<u>+0.75</u> (± 0.21)	<u>+0.73</u> (± 0.15)	<u>+0.86</u> (± 0.19)	-0.06 (± 0.12)	<u>-0.70</u> (± 0.78)	<u>+0.52</u> (± 0.37)
Passive Stereo		<u>+0.85</u> (± 0.16)	<u>+0.70</u> (± 0.18)	<u>+1.17</u> (± 0.05)	<u>+0.81</u> (± 0.25)	<u>-0.30</u> (± 0.44)	<u>+1.29</u> (± 0.18)

	Metric Type	Polystyrene Plate	Bunny Box	Bunny
RF ToF	C_g	2.10 (± 2.38)	0.32 (± 0.28)	0.28 (± 0.22)
NIR ToF		<u>3.28</u> (± 2.15)	<u>0.50</u> (± 0.29)	0.26 (± 0.14)
Active Stereo		3.01 (± 3.05)	0.39 (± 0.40)	0.12 (± 0.10)
Passive Stereo		2.99 (± 2.76)	0.39 (± 0.62)	0.08 (± 0.05)
RF ToF	C_s	0.14 (± 0.07)	0.30 (± 0.26)	<u>0.50</u> (± 0.41)
NIR ToF		2.50 (± 0.81)	0.48 (± 0.37)	0.31 (± 0.20)
Active Stereo		1.74 (± 1.97)	0.37 (± 0.35)	0.12 (± 0.09)
Passive Stereo		<u>2.92</u> (± 4.87)	<u>0.61</u> (± 1.08)	0.13 (± 0.13)
RF ToF	P	0.12 (± 0.10)	1.32 (± 2.45)	<u>0.74</u> (± 0.69)
NIR ToF		<u>17.95</u> (± 24.15)	<u>1.91</u> (± 2.83)	0.45 (± 1.77)
Active Stereo		10.63 (± 15.21)	0.99 (± 1.32)	0.16 (± 0.20)
Passive Stereo		10.08 (± 11.66)	1.05 (± 1.88)	0.17 (± 0.27)
RF ToF	P_e	0.12 (± 0.10)	1.12 (± 2.15)	<u>0.74</u> (± 0.69)
NIR ToF		<u>17.86</u> (± 24.12)	0.93 (± 0.87)	0.38 (± 0.12)
Active Stereo		10.48 (± 15.02)	1.46 (± 1.54)	0.11 (± 0.12)
Passive Stereo		9.81 (± 11.41)	<u>2.68</u> (± 2.54)	0.10 (± 0.12)
RF ToF	P^*	+0.11 (± 0.10)	+1.15 (± 2.45)	<u>+0.69</u> (± 0.69)
NIR ToF		<u>+17.95</u> (± 24.15)	<u>+1.73</u> (± 2.83)	-0.24 (± 1.77)
Active Stereo		+10.63 (± 15.21)	-0.83 (± 1.32)	-0.10 (± 0.20)
Passive Stereo		+10.08 (± 11.66)	-0.78 (± 1.88)	+0.08 (± 0.27)
RF ToF	P_e^*	+0.11 (± 0.10)	+1.03 (± 2.15)	<u>+0.69</u> (± 0.69)
NIR ToF		<u>+17.86</u> (± 24.12)	+0.92 (± 0.87)	-0.38 (± 0.12)
Active Stereo		+10.48 (± 15.02)	-1.46 (± 1.54)	-0.08 (± 0.12)
Passive Stereo		+9.81 (± 11.41)	<u>-2.48</u> (± 2.54)	+0.07 (± 0.12)

Table 9. We measure the sensor-GT deviation with respect to C_g , C_s , P , P_e and an additional signed version of P, P_e , which is denoted as P^*, P_e^* . All metrics are listed in the form ($\mu \pm \sigma$), consisting of the mean μ and standard deviation σ in centimeters, computed over the entire metric domain, respectively. The best results among all sensors of one metric type are highlighted in **bold** and the worst results are underlined.